Subgrid-scale modeling and implicit numerical dissipation in DG-based Large-Eddy Simulation

Subgrid-scale modeling and implicit numerical dissipation in DG-based Large-Eddy Simulation

P. Fernandez[*], N.C. Nguyen[†], J. Peraire [‡]

Massachusetts Institute of Technology, Cambridge, MA 02139, United States

Over the past few years, high-order discontinuous Galerkin (DG) methods for Large-Eddy Simulation (LES) have emerged as a promising approach to solve complex turbulent flows. However, despite the significant research investment, the relation between the discretization scheme, the subgrid-scale (SGS) model and the resulting LES solver remains unclear. This paper aims to shed some light on this matter. To that end, we investigate the role of the Riemann solver, the SGS model, the time resolution, and the accuracy order in the ability to predict a variety of flow regimes, including transition to turbulence, wall-free turbulence, wall-bounded turbulence, and turbulence decay. The transitional flow over the Eppler 387 wing, the Taylor-Green vortex problem and the turbulent channel flow are considered to this end. The focus is placed on post-processing the LES results and providing with a rationale for the performance of the various approaches.

I.   Introduction

Complete information about turbulent flows can be obtained by means of direct numerical simulation (DNS). Despite the availability of powerful supercomputers, DNS remains intractable for most practical applications. Large-Eddy Simulation (LES) is a viable alternative to DNS. The central premise of LES is that large-scale eddies dominate the turbulent transport and energy budget, so that a numerical simulation will provide a realistic depiction of the flow if it captures those scales explicitly and somehow accounts for the small scales that cannot be resolved. Strategies for dealing with the small turbulent scales include explicit subgrid-scale (SGS) modeling and implicit numerical dissipation.

In the classical (explicit) LES approach, the large-scale eddies of the flow field are resolved and the small scales are modeled using an SGS model. It turns out, however, that the leading-order term of the truncation error introduced by many numerical schemes is similar in form and magnitude to conventional SGS models. A natural alternative to the classical LES approach is therefore to use the numerical dissipation of the discretization scheme to account for the dissipation that takes place in the unresolved scales, leading to the so-called Implicit LES (ILES). The ILES approach was first introduced in 1990 by Boris et al.[4] and has been successfully applied with a number of different schemes, including finite volume methods,[13–15] standard[18] and compact[16,41] finite difference methods, spectral difference methods,[45] spectral/*hp* element methods,[21] flux reconstruction methods,[30] and disconstinuous Galerkin (DG) methods.[11,12,26,33,44] ILES benefits from its easy implementation without an SGS model and currently gains considerable attention from researchers in the computational fluid dynamics (CFD) community. This can be partially attributed to the fact that research has failed to shown an advantage of sophisticated SGS models over the *same-cost* LES with a simplistic model –or even with no model– and a slightly finer grid.[37]

In spite of the large effort on explicit and implicit SGS modeling in the last decades, it remains unclear how to best account for the effect of the subgrid scales. The lack of understanding of the relationship between the numerical scheme, the SGS model and the resulting LES solver is more evident for high-order DG methods; which are emerging as a promising approach for LES due to their ability to successfully predict complex turbulent flows.[11,33,39,44] This paper aims to shed some light on these questions and discuss the suitability and best practices for DG-based LES. We investigate the role of the Riemann solver, the explicit SGS model (if any), the time resolution, and the accuracy order in the resulting LES solver for a variety of flow regimes, including transition to turbulence, wall-free turbulence, wall-bounded turbulence, and turbulence decay. The transitional flow over the Eppler 387 wing,[23] the Taylor-Green vortex problem[38] and the turbulent channel flow[20] are considered to this end.

---

[*]PhD Student, Department of Aeronautics and Astronautics, MIT, AIAA Student Member.
[†]Principal Research Scientist, Department of Aeronautics and Astronautics, MIT, AIAA Member.
[‡]H.N. Slater Professor and Department Head of Aeronautics and Astronautics, MIT, AIAA Fellow.

American Institute of Aeronautics and Astronautics

The remainder of the paper is structured as follows. In Section II, we introduce the numerical discretization of the Navier-Stokes equations. Section III presents theoretical results on numerical dissipation and entropy stability of hybridized DG methods. In Section IV, we describe the subgrid-scale models and Riemann solvers considered in this work. Numerical results for the Eppler 387 wing, the Taylor-Green vortex problem and the turbulent channel flow are discussed in Sections V, VI and VII, respectively. Finally, we present some concluding remarks in Section VIII.

II.   Numerical discretization

A.   Governing equations

We consider the unsteady, compressible Navier-Stokes equations written in non-dimensional conservation form as

$$
\begin{aligned}
\boldsymbol{q} - \nabla \boldsymbol{u} &= 0, \quad \text{in } \Omega \times (0, T), \\
\frac{\partial \boldsymbol{u}}{\partial t} + \nabla \cdot \boldsymbol{F}(\boldsymbol{u}, \boldsymbol{q}) &= 0, \quad \text{in } \Omega \times (0, T).
\end{aligned}
\tag{1}
$$

Here, $\Omega \subseteq \mathbb{R}^d$ is a bounded physical domain with Lipschitz boundary $\partial \Omega$, $\boldsymbol{u} = (\rho, \rho v_j, \rho E) \in \Sigma \subseteq \mathbb{R}^m$, $j = 1, ..., d$ are the non-dimensional conserved quantities, and $\boldsymbol{F}(\boldsymbol{u}, \boldsymbol{q})$ are the Navier-Stokes fluxes of dimension $m \times d$,

$$
\boldsymbol{F}(\boldsymbol{u}, \boldsymbol{q}) = \boldsymbol{F}^{\mathcal{I}}(\boldsymbol{u}) + \boldsymbol{F}^{\mathcal{V}}(\boldsymbol{u}, \boldsymbol{q}) = \begin{pmatrix} \rho v_j \\ \rho v_i v_j + \delta_{ij} p \\ v_j(\rho E + p) \end{pmatrix} - \begin{pmatrix} 0 \\ \tau_{ij} \\ v_i \tau_{ij} + f_j \end{pmatrix}, \qquad i, j = 1, ..., d. \tag{2}
$$

For a Newtonian, calorically perfect gas in thermodynamic equilibrium, the non-dimensional viscous stress tensor, heat flux, and pressure are given by

$$
\tau_{ij} = \frac{1}{Re} \left[\left(\frac{\partial v_i}{\partial x_j} + \frac{\partial v_j}{\partial x_i} \right) - \frac{2}{3} \frac{\partial v_k}{\partial x_k} \delta_{ij} \right], \qquad f_j = -\frac{\gamma}{Re_\infty \, Pr} \frac{\partial T}{\partial x_j}, \qquad p = (\gamma - 1) \rho \left(E - \frac{1}{2} v_k \, v_k \right), \tag{3}
$$

respectively. Here, Re denotes the reference Reynolds number, Pr the Prandtl number, and γ the specific heat ratio. In particular, $Pr = 0.72$ and $\gamma = 1.4$ for air. In explicit LES, the viscous stress tensor is augmented with the subgrid-scale stress tensor, $\tau_{ij} \to \tau_{ij} + \tau_{ij}^{SGS}$; which is modeled through an SGS model. From a physical perspective, τ_{ij}^{SGS} accounts for the effect of the subgrid scales on the resolved scales. From a mathematical perspective, this is the extra-term that appears in the filtered Navier-Stokes equations that the resolved scales satisfy. While compressible flows also require modeling of the SGS heat transfer, SGS turbulent diffusion and SGS viscous diffusion, these additional terms are omitted here for simplicity of exposition.

B.   Numerical discretization

We consider high-order hybridized discontinuous Galerkin (DG) methods,[11] which generalize the HDG[7,27,31] and the EDG[7,8,32] methods, for the numerical simulation of turbulent flows. The hybridized DG discretization of the compressible Navier-Stokes equations reads as follows: Find $\left(\boldsymbol{q}_h(t), \boldsymbol{u}_h(t), \widehat{\boldsymbol{u}}_h(t) \right) \in \mathcal{Q}_h^k \times \mathcal{V}_h^k \times \mathcal{M}_h^k$ such that

$$
\left(\boldsymbol{q}_h, \boldsymbol{r}_h \right)_{\mathcal{T}_h} + \left(\boldsymbol{u}_h, \nabla \cdot \boldsymbol{r}_h \right)_{\mathcal{T}_h} - \left\langle \widehat{\boldsymbol{u}}_h, \boldsymbol{r}_h \cdot \boldsymbol{n} \right\rangle_{\partial \mathcal{T}_h} = 0, \tag{4a}
$$

$$
\left(\frac{\partial \boldsymbol{u}_h}{\partial t}, \boldsymbol{w}_h \right)_{\mathcal{T}_h} - \left(\boldsymbol{F}(\boldsymbol{u}_h, \boldsymbol{q}_h), \nabla \boldsymbol{w}_h \right)_{\mathcal{T}_h} + \left\langle \widehat{\boldsymbol{f}}_h(\widehat{\boldsymbol{u}}_h, \boldsymbol{u}_h, \boldsymbol{q}_h), \boldsymbol{w}_h \right\rangle_{\partial \mathcal{T}_h} = 0, \tag{4b}
$$

$$
\left\langle \widehat{\boldsymbol{f}}_h(\widehat{\boldsymbol{u}}_h, \boldsymbol{u}_h, \boldsymbol{q}_h), \boldsymbol{\mu} \right\rangle_{\partial \mathcal{T}_h \backslash \partial \Omega} + \left\langle \widehat{\boldsymbol{b}}_h(\widehat{\boldsymbol{u}}_h, \boldsymbol{u}_h, \boldsymbol{q}_h), \boldsymbol{\mu} \right\rangle_{\partial \Omega} = 0, \tag{4c}
$$

for all $(\boldsymbol{r}_h, \boldsymbol{w}_h, \boldsymbol{\mu}_h) \in \mathcal{Q}_h^k \times \mathcal{V}_h^k \times \mathcal{M}_h^k$ and all $t \in (0, T)$. The nomenclature, finite element spaces and inner products above are described in Appendix A. The numerical flux $\widehat{\boldsymbol{f}}_h$ in Eq. (4) is defined as

$$
\widehat{\boldsymbol{f}}_h(\widehat{\boldsymbol{u}}_h, \boldsymbol{u}_h, \boldsymbol{q}_h; \boldsymbol{n}) = \boldsymbol{F}^{\mathcal{I}}(\widehat{\boldsymbol{u}}_h) \cdot \boldsymbol{n} + \boldsymbol{F}^{\mathcal{V}}(\widehat{\boldsymbol{u}}_h, \boldsymbol{q}_h) \cdot \boldsymbol{n} + \boldsymbol{\sigma}(\widehat{\boldsymbol{u}}_h, \boldsymbol{u}_h; \boldsymbol{n}) \cdot (\boldsymbol{u}_h - \widehat{\boldsymbol{u}}_h). \tag{5}
$$

We note that this form of the numerical flux does not involve an explicit Riemann solver. Instead, it is the so-called stabilization matrix $\boldsymbol{\sigma}(\widehat{\boldsymbol{u}}_h, \boldsymbol{u}_h; \boldsymbol{n})$ that implicitly defines the Riemann solver in hybridized DG methods. The semi-discrete system (4) is further discretized in time using L-stable, diagonally implicit Runge-Kutta (DIRK) schemes.[1] A description of the parallel iterative solver used for the resulting nonlinear system of equations can be found in.[9–11]

American Institute of Aeronautics and Astronautics

III. Numerical dissipation and entropy stability analysis for hybridized DG methods

Hybridized DG methods are a new, promising approach for high-fidelity CFD, including large-eddy simulation, due to the reduced number of globally coupled unknowns and memory footprint with respect to standard DG methods.[11,28] However, little is known about the Riemann flux, numerical dissipation and entropy stability in this family of schemes. In this section, we present theoretical results for the discretization of the convective operator of the Navier-Stokes equations; which apply more generally to hyperbolic systems of conservation laws.

A. Riemann solver

The following result on the connection between the stabilization matrix $\boldsymbol{\sigma}$ and the resulting Riemann flux $\widehat{\boldsymbol{f}}_h$ holds for hyperbolic systems of conservation laws.

Proposition 1 *Let F be a face in $\mathcal{E}_h^I \cap \mathcal{E}_h^H$ and let $\boldsymbol{F}^{\mathcal{I}}$ denote the flux of a hyperbolic system of conservation laws. The numerical flux in hybridized DG methods, Eq. (5), implicitly defines a linearized Riemann solver between the left $\boldsymbol{u}_h^-$ and right $\boldsymbol{u}_h^+$ states of F whose numerical flux is given by*

$$\widehat{\boldsymbol{f}}_h^{\pm} = \frac{1}{2}\big(\boldsymbol{F}^{\mathcal{I}}(\boldsymbol{u}_h^-) + \boldsymbol{F}^{\mathcal{I}}(\boldsymbol{u}_h^+)\big) \cdot \boldsymbol{n}^{\pm} - \frac{1}{2}\boldsymbol{\mathcal{D}}(\boldsymbol{u}_h^{\mp}, \boldsymbol{u}_h^{\pm}; \boldsymbol{n}^{\pm}) \cdot \big(\boldsymbol{u}_h^{\mp} - \boldsymbol{u}_h^{\pm}\big), \tag{6}$$

where the dissipation matrix $\boldsymbol{\mathcal{D}} \in \mathbb{R}^{m \times m}$ is of the form

$$\begin{aligned}
\boldsymbol{\mathcal{D}}(\boldsymbol{u}_1, \boldsymbol{u}_2; \boldsymbol{n}) = {}& \boldsymbol{\sigma}(\widehat{\boldsymbol{u}}, \boldsymbol{u}_2; \boldsymbol{n}) \cdot \Big(\frac{1}{2}\big(\boldsymbol{\sigma}(\widehat{\boldsymbol{u}}, \boldsymbol{u}_1; -\boldsymbol{n}) + \boldsymbol{\sigma}(\widehat{\boldsymbol{u}}, \boldsymbol{u}_2; \boldsymbol{n})\big)\Big)^{-1} \cdot \boldsymbol{\sigma}(\widehat{\boldsymbol{u}}, \boldsymbol{u}_1; -\boldsymbol{n}) \\
&+ \boldsymbol{\mathcal{A}}_n(\boldsymbol{u}_1, \widehat{\boldsymbol{u}}; \boldsymbol{n}) \cdot \big(\boldsymbol{\sigma}(\widehat{\boldsymbol{u}}, \boldsymbol{u}_1; -\boldsymbol{n}) + \boldsymbol{\sigma}(\widehat{\boldsymbol{u}}, \boldsymbol{u}_2; \boldsymbol{n})\big)^{-1} \cdot \boldsymbol{\sigma}(\widehat{\boldsymbol{u}}, \boldsymbol{u}_2; \boldsymbol{n}) \\
&- \boldsymbol{\mathcal{A}}_n(\boldsymbol{u}_2, \widehat{\boldsymbol{u}}; \boldsymbol{n}) \cdot \big(\boldsymbol{\sigma}(\widehat{\boldsymbol{u}}, \boldsymbol{u}_1; -\boldsymbol{n}) + \boldsymbol{\sigma}(\widehat{\boldsymbol{u}}, \boldsymbol{u}_2; \boldsymbol{n})\big)^{-1} \cdot \boldsymbol{\sigma}(\widehat{\boldsymbol{u}}, \boldsymbol{u}_1; -\boldsymbol{n}).
\end{aligned} \tag{7}$$

Here, $\boldsymbol{\mathcal{A}}_n(\boldsymbol{u}, \widehat{\boldsymbol{u}}; \boldsymbol{n}) = \int_0^1 \boldsymbol{A}_n\big(\tilde{\boldsymbol{u}}(\theta; \boldsymbol{u}, \widehat{\boldsymbol{u}}); \boldsymbol{n}\big)\,d\theta$, $\boldsymbol{A}_n = \big(\partial\boldsymbol{F}^{\mathcal{I}}/\partial\boldsymbol{u}\big) \cdot \boldsymbol{n}$, $\tilde{\boldsymbol{u}}(\theta; \boldsymbol{u}_a, \boldsymbol{u}_b) = \boldsymbol{u}_a + \theta(\boldsymbol{u}_b - \boldsymbol{u}_a)$, and the numerical trace $\widehat{\boldsymbol{u}}_h$ is implicitly given by

$$\widehat{\boldsymbol{u}}_h = \big(\boldsymbol{\sigma}(\widehat{\boldsymbol{u}}_h, \boldsymbol{u}_h^-; \boldsymbol{n}^-) + \boldsymbol{\sigma}(\widehat{\boldsymbol{u}}_h, \boldsymbol{u}_h^+; \boldsymbol{n}^+)\big)^{-1} \cdot \big(\boldsymbol{\sigma}(\widehat{\boldsymbol{u}}_h, \boldsymbol{u}_h^-; \boldsymbol{n}^-) \cdot \boldsymbol{u}_h^- + \boldsymbol{\sigma}(\widehat{\boldsymbol{u}}_h, \boldsymbol{u}_h^+; \boldsymbol{n}^+) \cdot \boldsymbol{u}_h^+\big). \tag{8}$$

Equations (6), (7) and (8) hold in a weak sense $\langle \, \cdot \, , \boldsymbol{\mu}\rangle_F$ for any $\boldsymbol{\mu} \in \mathcal{M}_h^k|_F$.

The appearance of the second and third terms in the right-hand side of Eq. (7) is due to the definition of the numerical flux in hybridized DG methods in terms of $\boldsymbol{F}^{\mathcal{I}}(\widehat{\boldsymbol{u}}_h)$, as opposed to $\big(\boldsymbol{F}^{\mathcal{I}}(\widehat{\boldsymbol{u}}_h) + \boldsymbol{F}^{\mathcal{I}}(\boldsymbol{u}_h)\big)/2$ as in linearized Riemann solvers. Also, in the particular case of the compressible Euler equations, $\boldsymbol{\mathcal{A}}_n(\boldsymbol{u}_1, \boldsymbol{u}_2; \boldsymbol{n}) = \boldsymbol{A}_n(\boldsymbol{u}_{Roe}(\boldsymbol{u}_1, \boldsymbol{u}_2); \boldsymbol{n})$, where $\boldsymbol{u}_{Roe}(\boldsymbol{u}_1, \boldsymbol{u}_2)$ denotes the Roe state.[34]

Corollary 1 *If $\boldsymbol{\sigma}^{\pm}$ are non-defective, share eigenvectors, and $(\boldsymbol{\sigma}^- + \boldsymbol{\sigma}^+)$ is non-singular, then $\widehat{\boldsymbol{u}}_h$ is given by a convex combination of $\boldsymbol{u}_h^-$ and $\boldsymbol{u}_h^+$ in each eigenspace. In particular, this is the case if $\boldsymbol{\sigma} = \tilde{\boldsymbol{\sigma}}(\boldsymbol{A}_n(\widehat{\boldsymbol{u}}_h))$ is a function of $\boldsymbol{A}_n(\widehat{\boldsymbol{u}}_h)$, where $\tilde{\boldsymbol{\sigma}} \in \mathcal{C}^0(\mathrm{Sp}[\boldsymbol{A}_n(\widehat{\boldsymbol{u}}_h)])$ is a continuous function on the spectrum of $\boldsymbol{A}_n(\widehat{\boldsymbol{u}}_h)$. In this case, the eigenvectors of $\boldsymbol{\sigma}^{\pm}$ correspond to characteristic variables, where the conservative-to-characteristic change of variables is that at the state $\widehat{\boldsymbol{u}}_h$.*

B. Entropy stability analysis

Let $\big(H(\boldsymbol{u}), \boldsymbol{\mathcal{F}}^{\mathcal{I}}(\boldsymbol{u})\big)$ denote a generalized entropy pair for the inviscid operator of the Navier-Stokes system, where $H(\boldsymbol{u}) : \mathbb{R}^m \to \mathbb{R}$ is a convex entropy function and $\boldsymbol{\mathcal{F}}^{\mathcal{I}}(\boldsymbol{u}) : \mathbb{R}^m \to \mathbb{R}^d$ is the corresponding entropy flux that satisfies

$$\frac{\partial \mathcal{F}_i^{\mathcal{I}}}{\partial u_j} = \frac{\partial H}{\partial u_k}\frac{\partial F_{ik}^{\mathcal{I}}}{\partial u_j}, \qquad i = 1, ..., d, \quad j, k = 1, ..., m. \tag{9}$$

The following entropy stability results hold for entropy-variable-based formulations.

Proposition 2 (Semi-discrete global entropy stability) *The time evolution of generalized entropy in hybridized DG methods is given by*

$$\frac{d}{dt} \int_{\mathcal{T}_h} H(\boldsymbol{v}_h) + \int_{\partial \mathcal{T}_h^I} (\boldsymbol{v}_h - \widehat{\boldsymbol{v}}_h)^t \cdot \left[\boldsymbol{\sigma}(\widehat{\boldsymbol{v}}_h, \boldsymbol{v}_h; \boldsymbol{n}) - \frac{1}{2} \boldsymbol{\mathcal{A}}_n(\widehat{\boldsymbol{v}}_h, \boldsymbol{v}_h; \boldsymbol{n}) - \tilde{\boldsymbol{\Lambda}}_n(\widehat{\boldsymbol{v}}_h, \boldsymbol{v}_h; \boldsymbol{n}) \right] \cdot (\boldsymbol{v}_h - \widehat{\boldsymbol{v}}_h)$$
$$+ \mathcal{B}_{\partial\Omega}^{hDG}(\widehat{\boldsymbol{v}}_h, \boldsymbol{v}_h; \boldsymbol{v}^{\partial\Omega}) = 0, \tag{10}$$

where $\boldsymbol{v}_h$ denotes entropy variables,

$$\mathcal{B}_{\partial\Omega}^{hDG}(\widehat{\boldsymbol{v}}_h, \boldsymbol{v}_h; \boldsymbol{v}^{\partial\Omega}) = \int_{\partial\Omega} \boldsymbol{\mathcal{F}}_n^{\mathcal{I}}(\boldsymbol{v}_h) + \int_{\partial\Omega} \boldsymbol{v}_h^t \cdot \left(\widehat{\boldsymbol{f}}_h(\widehat{\boldsymbol{v}}_h, \boldsymbol{v}_h) - \boldsymbol{F}_n^{\mathcal{I}}(\boldsymbol{v}_h) \right) - \int_{\partial\Omega} \widehat{\boldsymbol{v}}_h^t \cdot \widehat{\boldsymbol{b}}_h(\widehat{\boldsymbol{v}}_h, \boldsymbol{v}_h; \boldsymbol{v}^{\partial\Omega})$$

is a boundary term whose precise form depends on the type of boundary conditions, $\boldsymbol{v}^{\partial\Omega}$ is a boundary state with support on $\partial\Omega$,

$$\tilde{\boldsymbol{\Lambda}}_n(\boldsymbol{v}_1, \boldsymbol{v}_2; \boldsymbol{n}) = \frac{1}{2} \int_0^1 (1-\theta) \left(\tilde{\boldsymbol{A}}_n(\tilde{\boldsymbol{v}}(\theta; \boldsymbol{v}_1, \boldsymbol{v}_2); \boldsymbol{n}) - \tilde{\boldsymbol{A}}_n(\tilde{\boldsymbol{v}}(\theta; \boldsymbol{v}_2, \boldsymbol{v}_1); \boldsymbol{n}) \right) d\theta$$
$$= \frac{1}{2} \int_0^1 (1-2\theta) \tilde{\boldsymbol{A}}_n(\tilde{\boldsymbol{v}}(\theta; \boldsymbol{v}_1, \boldsymbol{v}_2); \boldsymbol{n}) d\theta = -\frac{1}{2} \int_0^1 (1-2\theta) \tilde{\boldsymbol{A}}_n(\tilde{\boldsymbol{v}}(\theta; \boldsymbol{v}_2, \boldsymbol{v}_1); \boldsymbol{n}) d\theta, \tag{11}$$

$\tilde{\boldsymbol{A}}_n = \boldsymbol{A}_n \tilde{\boldsymbol{A}}_0$, *and* $\tilde{\boldsymbol{A}}_0 = \partial \boldsymbol{u}/\partial \boldsymbol{v}$.

Corollary 2 *Any stabilization matrix satisfying*

$$(\boldsymbol{v}_h - \widehat{\boldsymbol{v}}_h)^t \cdot \boldsymbol{\sigma}(\widehat{\boldsymbol{v}}_h, \boldsymbol{v}_h; \boldsymbol{n}) \cdot (\boldsymbol{v}_h - \widehat{\boldsymbol{v}}_h) \geq (\boldsymbol{v}_h - \widehat{\boldsymbol{v}}_h)^t \cdot \boldsymbol{\sigma}_{MV}^{hDG}(\widehat{\boldsymbol{v}}_h, \boldsymbol{v}_h; \boldsymbol{n}) \cdot (\boldsymbol{v}_h - \widehat{\boldsymbol{v}}_h), \tag{12}$$

for all $(\widehat{\boldsymbol{v}}_h, \boldsymbol{v}_h) \in \Sigma \otimes \Sigma$ and $|\boldsymbol{n}| = 1$, leads to an entropy-stable (continuous-time) hybridized DG discretization. Here,

$$\boldsymbol{\sigma}_{MV}^{hDG}(\boldsymbol{v}_1, \boldsymbol{v}_2; \boldsymbol{n}) = \frac{1}{2} \boldsymbol{\mathcal{A}}_n(\boldsymbol{v}_1, \boldsymbol{v}_2; \boldsymbol{n}) + \frac{1}{2} \int_0^1 (1-\theta) \left(\left| \tilde{\boldsymbol{A}}_n(\tilde{\boldsymbol{v}}(\theta; \boldsymbol{v}_1, \boldsymbol{v}_2); \boldsymbol{n}) \right|_{\tilde{\boldsymbol{A}}_0} + \left| \tilde{\boldsymbol{A}}_n(\tilde{\boldsymbol{v}}(\theta; \boldsymbol{v}_2, \boldsymbol{v}_1); \boldsymbol{n}) \right|_{\tilde{\boldsymbol{A}}_0} \right) d\theta$$
$$= \frac{1}{2} \boldsymbol{\mathcal{A}}_n(\boldsymbol{v}_1, \boldsymbol{v}_2; \boldsymbol{n}) + \frac{1}{2} \int_0^1 \left| \tilde{\boldsymbol{A}}_n(\tilde{\boldsymbol{v}}(\theta; \boldsymbol{v}_1, \boldsymbol{v}_2); \boldsymbol{n}) \right|_{\tilde{\boldsymbol{A}}_0} d\theta$$
$$= \frac{1}{2} \boldsymbol{\mathcal{A}}_n(\boldsymbol{v}_1, \boldsymbol{v}_2; \boldsymbol{n}) + \frac{1}{2} \int_0^1 \left| \tilde{\boldsymbol{A}}_n(\tilde{\boldsymbol{v}}(\theta; \boldsymbol{v}_2, \boldsymbol{v}_1); \boldsymbol{n}) \right|_{\tilde{\boldsymbol{A}}_0} d\theta, \tag{13}$$

and $\left| \tilde{\boldsymbol{A}}_n \right|_{\tilde{\boldsymbol{A}}_0} := \tilde{\boldsymbol{A}}_0 \left| \tilde{\boldsymbol{A}}_0^{-1} \tilde{\boldsymbol{A}}_n \right| \equiv |\boldsymbol{A}_n| \tilde{\boldsymbol{A}}_0$ is the generalized absolute value operator with respect to the metric tensor $\tilde{\boldsymbol{A}}_0$.

We recall that the time evolution of generalized entropy in a standard DG method with a linearized Riemann flux reads as[2]

$$\frac{d}{dt} \int_{\mathcal{T}_h} H + \int_{\mathcal{E}_h^I} (\boldsymbol{v}_h^+ - \boldsymbol{v}_h^-)^t \cdot \left(\boldsymbol{\mathcal{D}}(\boldsymbol{v}_h^-, \boldsymbol{v}_h^+; \boldsymbol{n}^+) - \tilde{\boldsymbol{\Lambda}}_n(\boldsymbol{v}_h^-, \boldsymbol{v}_h^+; \boldsymbol{n}^+) \right) \cdot (\boldsymbol{v}_h^+ - \boldsymbol{v}_h^-) + \mathcal{B}_{\partial\Omega}^{DG}(\boldsymbol{v}_h) = 0, \tag{14}$$

where the boundary operator $\mathcal{B}_{\partial\Omega}^{DG}$ is similar in form to $\mathcal{B}_{\partial\Omega}^{hDG}$. The entropy generation and thus numerical dissipation due to inter-element jumps in hybridized DG methods is analogous in form to that in standard DG methods. As such, most theoretical results on DG and Riemann solvers carry over to the hybridized framework.

IV. Riemann solvers and explicit SGS models

A. Riemann solvers

We consider the three following choices of stabilization matrix:

$$\boldsymbol{\sigma} = \frac{1}{2} \left(\boldsymbol{A}_n(\widehat{\boldsymbol{u}}_h) + |\boldsymbol{A}_n(\widehat{\boldsymbol{u}}_h)| \right), \qquad \boldsymbol{\sigma} = |\boldsymbol{A}_n(\widehat{\boldsymbol{u}}_h)|, \qquad \boldsymbol{\sigma} = \lambda_{max}(\widehat{\boldsymbol{u}}_h) \, \boldsymbol{I}, \tag{15}$$

American Institute of Aeronautics and Astronautics

where I is the $m \times m$ identity matrix and λ_{max} denotes the maximum-magnitude eigenvalue of A_n. In practice, $(\cdot + |\cdot|)/2$ and $|\cdot|$ are replaced by the smooth surrogates

$$\frac{1}{2}(x+|x|) \longrightarrow (x-\epsilon)\left(\frac{\operatorname{atan}\big(b(x-\epsilon)\big)}{\pi} + \frac{1}{2}\right) - \frac{\operatorname{atan}(b)}{\pi} + \frac{1}{2} + \epsilon \approx \max\left\{\frac{1}{2}(x+|x|), \epsilon\right\}, \qquad b = 10, \quad (16a)$$

$$|x| \longrightarrow 2\left[(x-\epsilon)\left(\frac{\operatorname{atan}\big(b(x-\epsilon)\big)}{\pi} + \frac{1}{2}\right) - \frac{\operatorname{atan}(b)}{\pi} + \frac{1}{2}\right] - x + \epsilon \approx \max\{|x|, \epsilon\}, \qquad b = 10, \quad (16b)$$

respectively, in order to improve the robustness of the nonlinear solver. Also, $0 < \epsilon$ $(<< \lambda_{min})$ is used to provide some stabilization in the outgoing characteristic fields and improve linear and nonlinear stability. This can be interpreted as an entropy fix.

For linear hyperbolic systems of conservation laws, $(A_n + |A_n|)/2$ and $|A_n|$ lead to upwinded numerical flux and upwinded numerical trace, and upwinded numerical flux and centered numerical trace, respectively. Also, $(A_n + |A_n|)/2$ and $|A_n|$ result in the same numerical solution for linear problems. This is not the case, however, in the nonlinear setting. In addition, the discrete systems obtained with both choices have different stability properties; which may lead to significant differences in the performance of iterative solvers.

B.   Subgrid-scale models

We consider the Smagorinsky,[36] WALE[29] and Vreman[42] explicit subgrid-scale models. As eddy-viscosity models, the deviatoric part of the (dimensional) SGS tensor is of the form

$$\tau_{ij}^{SGS} - (1/3)\,\tau_{kk}^{SGS}\,\delta_{ij} = 2\rho\nu_e\,S_{ij}, \tag{17}$$

where ν_e is the so-called (kinematic) eddy viscosity and $S_{ij} = (J_{ij} + J_{ji})/2$ is the symmetric part of the resolved velocity gradient tensor $J_{ij} = \partial v_i / \partial x_j$. The eddy viscosity in the Smagorinsky, WALE and Vreman models is given by

$$\text{Smagorinsky:} \qquad \nu_e^S = (C_s\Delta)^2\,(2\,S_{pq}S_{pq})^{1/2}, \tag{18a}$$

$$\text{WALE:} \qquad \nu_e^W = (C_w\Delta)^2\,\frac{(W_{ij}^d W_{ij}^d)^{3/2}}{(S_{pq}S_{pq})^{5/2} + (W_{ij}^d W_{ij}^d)^{5/4}}, \tag{18b}$$

$$\text{Vreman:} \qquad \nu_e^V = (C_v\Delta)^2\left(\frac{Q_G}{J_{ij}J_{ij}}\right)^{1/2}. \tag{18c}$$

Here, $C_s = 0.16$,[17,22] $C_w = 0.50$[29] and $C_v = 0.26$[42] are model constants, Δ is a characteristic element length, W_{ij}^d denotes the deviatoric part of $W_{ij} = S_{ik}S_{kj} + R_{ik}R_{kj}$, where R_{ij} is the skew-symmetric part of J_{ij}, and $Q_G = (G_{kk}^2 - G_{ij}G_{ji})/2$ is the second invariant of the tensor $G_{ij} = J_{ik}J_{jk}$. The length scale is defined as $\Delta = V_K^{1/3}/k$, where V_K is the element volume and k the polynomial order of the numerical approximation. Unlike in the Smagorinsky model, the eddy viscosity in Vreman and (to a lessen extent) WALE vanishes for many laminar flow types,[42] including the viscous sublayer of a turbulent boundary layer.

In compressible turbulence, the isotropic part of the subgrid-scale stress tensor, as well as the SGS heat transfer, SGS turbulent diffusion and SGS viscous diffusion, also need to be modeled. To that end, the Yoshizawa model[43] is used for the isotropic part of the SGS stress tensor, whereas the subgrid-scale heat transfer and turbulent diffusion are modeled through an SGS eddy Prandtl number $Pr_e = 0.7$ approach and the model by Knight et al.,[19] respectively. The SGS viscous diffusion is neglected due to its small magnitude compared to the subgrid-scale heat transfer and turbulent diffusion.

V.   The Eppler 387 wing

A.   Case description

First, we examine the ability of explicit and implicit LES approaches to resolve transition from laminar to turbulent regime. To this end, we consider the Eppler 387 wing at Reynolds number of 300,000. The angle of attack is set to $\alpha = 4.0°$, the Mach number to $M_\infty = 0.09$, and the freestream turbulence intensity to $I_\infty = 0.0$. As it happens, the experimental data for the Eppler wing[23] are arguably the most accurate and reliable in the literature of transitional flows. This justifies the choice of this test case here.

B. Details of the numerical discretization

The HDG method and the DIRK(3,3) scheme are used for the spatial and temporal discretization of the Navier-Stokes equations, respectively. The stabilization matrix is $\sigma = \lambda_{max}$ and the polynomial degree of the numerical approximation $k = 4$, hence yielding a scheme that is fifth-order accurate in space and third-order accurate in time. The computational domain is partitioned using isoparametric tetrahedral elements. The extrusion length in the spanwise direction is $0.1c$ and the computational domain extends about 10 chords away from the wing in the radial direction. Due to the chaotic dynamics in LES, the simulation time is sufficiently large to ensure statistical convergence of the transition location. In particular, the simulation is considered statistically converged to this end when the L^2-norm of the covariance field of the spanwise- and time-averaged pressure coefficient on the airfoil is below $2c \cdot 0.01$. The variance of an LES estimator is computed from the instantaneous fields and the *weak dependence* version of the central limit theorem.[3]

C. Grid convergence study

We perform a grid convergence study with ILES in order to estimate the resolution required to capture transition. To this end, a sequence of finer and finer meshes are considered until the transition location and the pressure coefficient are grid independent and thus *grid converged*. The simulation is considered grid converged for this purpose when both the L^2-norm of the difference of spanwise- and time-averaged pressure coefficient between consecutive meshes is below $2c \cdot 0.005$, and the difference in the transition location is below $0.0025c$. This leads to the three meshes and non-dimensional time steps in Table 1; which correspond to uniform refinement in space and time.

The negative spanwise- and time-averaged pressure coefficients are shown in Figure 1. The ILES results agree very well with the experimental data reported in,[23] and display grid convergence as the mesh is refined. In particular, the error in the transition location with respect to the experimental data is below $0.01c$ for all meshes and grid convergence as defined above is achieved with mesh No. 2. This is therefore the resolution that will be used for the comparison of explicit and implicit LES approaches in the section below. A 2D slice of this mesh is shown in Figure 2. We note

Mesh No.	k	No. Elements	Element type	$\Delta t\, U_\infty/c$
1	4	$64,800$	Tetrahedra	$7.937 \cdot 10^{-3}$
2	4	$126,360$	Tetrahedra	$6.300 \cdot 10^{-3}$
3	4	$254,976$	Tetrahedra	$5.000 \cdot 10^{-3}$

Table 1: Details of the computational meshes considered for the Eppler 387 wing.
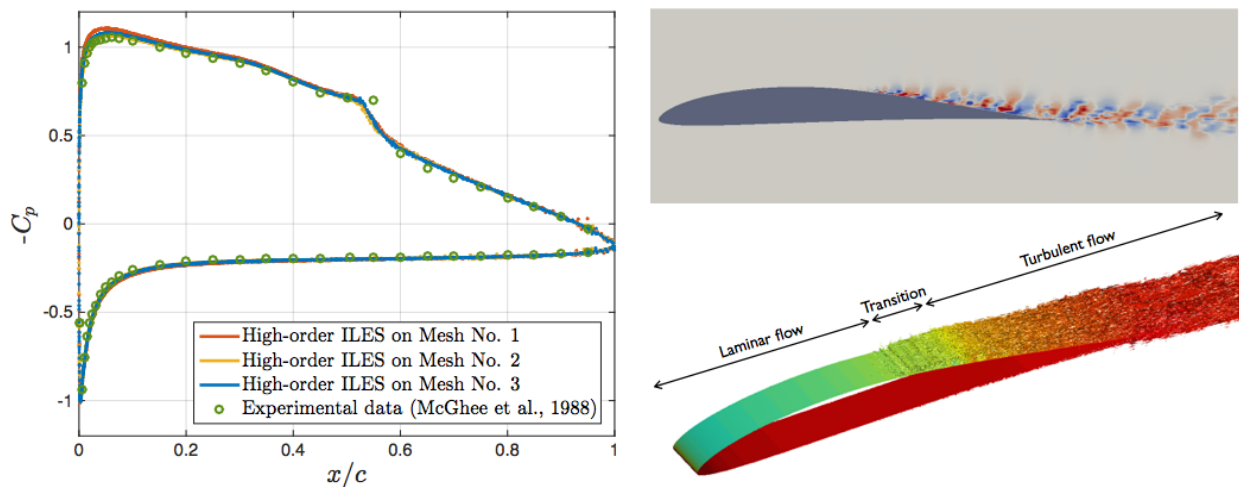

Figure 1: ILES predictions of the transitional flow over the Eppler 387 wing: Pressure coefficient (left), instantaneous spanwise velocity (top right), and iso-surface of the Q-criterion colored by pressure (bottom right).
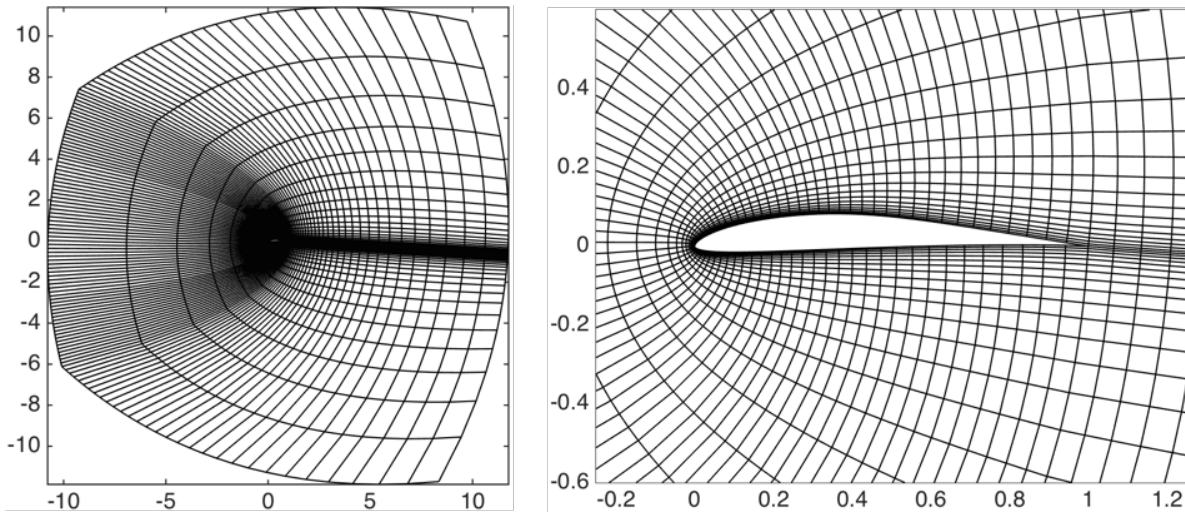
Figure 2: 2D slice of mesh No. 2 for the Eppler 387 wing. The tetrahedral mesh is created by subdividing each hexahedron into 6 tetrahedra.

that the effective resolution of mesh No. 2 is equivalent to a cell-centered finite volume discretization with 1.3 million elements; which is much below that typically needed to capture transition with low-order methods.

D. Explicit vs. implicit LES

Figure 3 shows the pressure coefficient predicted by ILES, Smagorinsky-LES and Vreman-LES. Also, Table 2 collects the separation and reattachment locations on the suction side boundary layer (BL), and Figure 4 displays the spanwise- and time-averaged velocity magnitude field. WALE-LES leaded to nonlinear instability and the breakdown of the iterative solver; which is attributed to the stiffness of the problem due to both model nonlinearity and the high-order discretization.

The Smagorinsky model provides a very poor description of the flow due to the eddy viscosity failing to vanish near the wall, as discussed in Section IV. As a result, Smagorinsky-LES effectively solves a lower Reynolds number flow. This leads to the large separation bubble on the suction side in Fig. 4 and the corresponding pressure plateau in Fig. 3; which is characteristic of the Eppler 387 wing at lower Reynolds numbers.[11,23] Hence, the Smagorinsky model, in its standard form, is not able to predict boundary layer transition and is thus not well suited for transitional flows.

We further investigate the transition prediction capability of ILES and Vreman-LES by analyzing the boundary layer structure and the transition mechanism in both simulations. The methodology for the BL analysis is presented in Appendix B. Since the large separation in Smagorinsky-LES dramatically changes the potential flow around the airfoil, and thus the pressure gradient felt by the boundary layer, no conclusions can be inferred on this model from the BL analysis. Hence, the results are omitted here.

From a qualitative perspective, the structure of the boundary layer is the same (and consistent with the experimental data) both in ILES and Vreman-LES. On the pressure side, the boundary layer remains attached all the way until the trailing edge. In particular, the design of the Eppler 387 wing is such that the adverse pressure gradient on the lower

	x_s/c	x_r/c
ILES	0.458	0.553
Smagorinsky-LES	0.329	0.560
Vreman-LES	0.466	0.568

Table 2: Separation and reattachment location on the suction side in ILES, Smagorinsky-LES and Vreman-LES for the Eppler 387 wing.

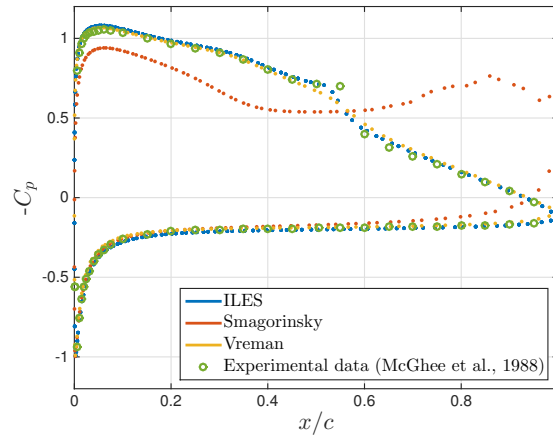American Institute of Aeronautics and Astronautics

Figure 3: Spanwise- and time-averaged pressure coefficient in ILES, Smagorinsky-LES and Vreman-LES for the Eppler 387 wing.

side takes place only in a very small region near the leading edge, where the momentum thickness is small and the boundary layer therefore very resistant to separation. The greater stability of the attached BL translates into a fully laminar flow along the pressure side despite the relatively large value of the Reynolds number. On the suction side, however, the flow separates due to the adverse pressure gradient. This produces a laminar separation bubble (LSB) and strongly destabilizes the boundary layer; which rapidly transitions to turbulence. After transition, the turbulent mixing leads to the reattachment of the boundary layer and the end of the separation bubble. The turbulent BL then remains
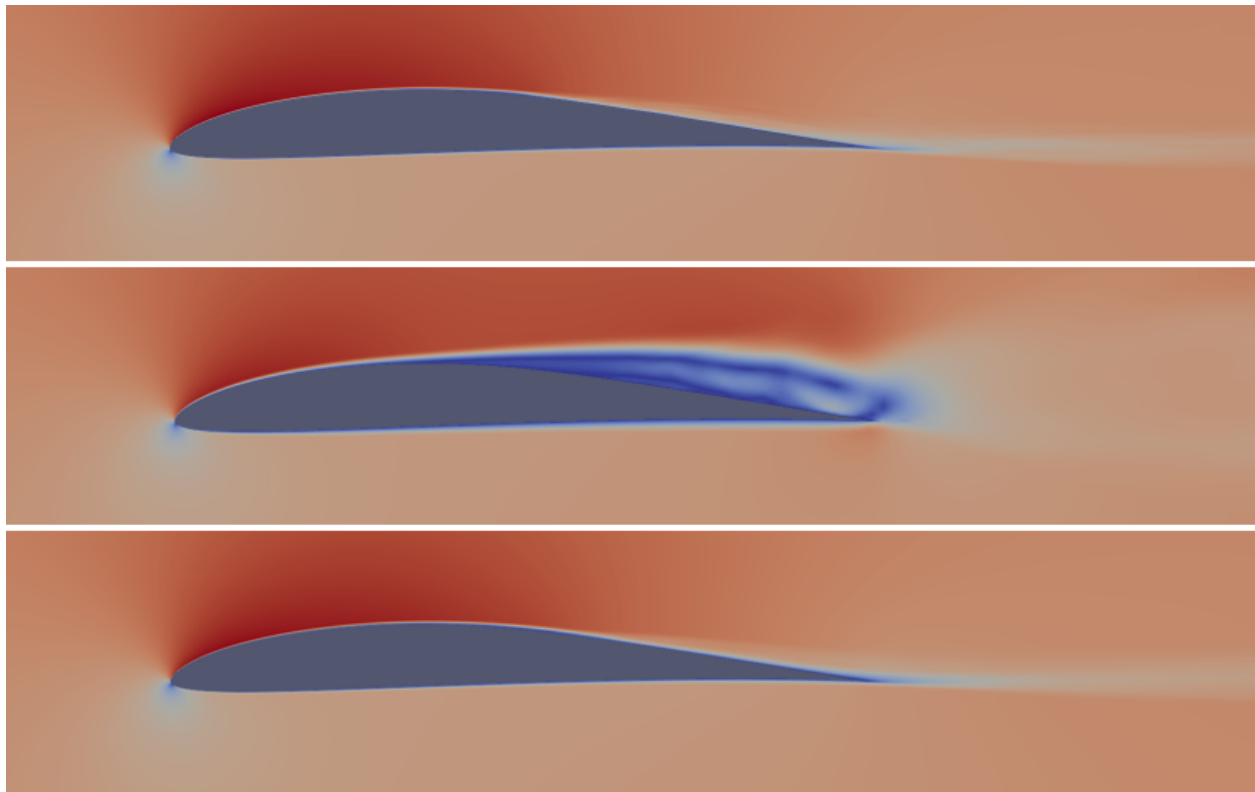
Figure 4: Spanwise- and time-averaged velocity magnitude field computed in ILES (top), Smagorinsky-LES (middle) and Vreman-LES (bottom) for the Eppler 387 wing.

American Institute of Aeronautics and Astronautics
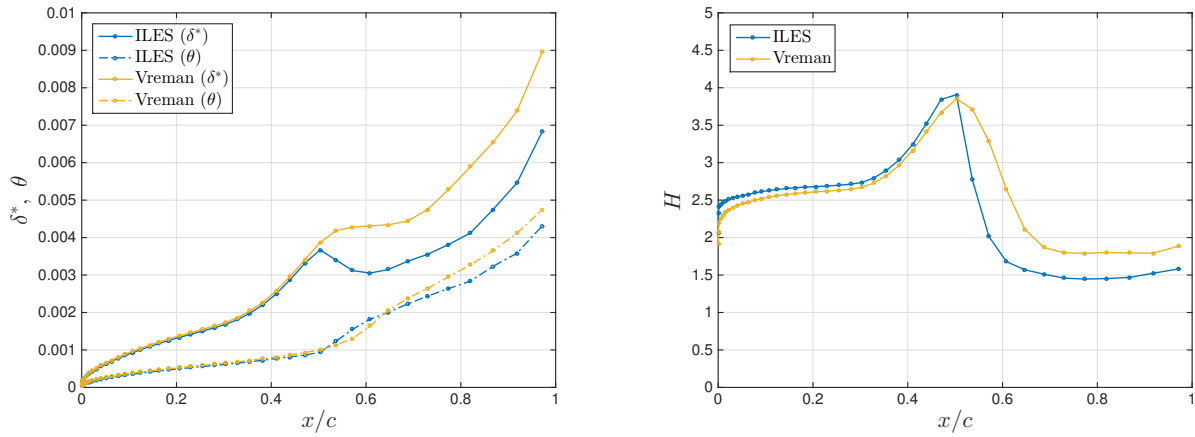
Figure 5: ILES and Vreman-LES predictions of streamwise displacement and momentum thickness (left) and shape parameter (right) along the suction side of the Eppler 387 wing.

attached all the way until the trailing edge thanks to the resistance to separation provided by the turbulent mixing. The LSB translates into a small pressure plateau, followed by a rapid pressure rise after transition, as illustrated in Fig. 3. This plateau is a consequence of the nearly-still fluid inside the laminar part of the bubble being unable to sustain any significant pressure gradients. The turbulent mixing in the turbulent portion of the bubble, however, can support the subsequent strong adverse pressure gradient. Also, BL separation leads to an increase in the displacement thickness and thus the shape parameter, as illustrated in Fig. 5. The increase in the shape parameter is (indirectly) responsible for the rapid growth of instabilities along the bubble, as discussed below. The large value of the displacement thickness along the adverse pressure gradient in the turbulent portion of the bubble is responsible for the so-called *bubble drag*. Once the LSB ends, the shape parameter reduces back to attached regime values. The adverse pressure gradient from the reattachment location to the trailing edge leads to the final increase in the displacement and momentum thickness in Figure 5.

Due to the lack of bypass and forced transition mechanisms and the quasi-2D nature of the flow, natural transition through two-dimensional unstable modes is expected. This is numerically confirmed both by the ILES and Vreman-LES results. The two-dimensional nature of transition is illustrated in Fig. 6 through the much larger amplitude of the streamwise instabilities compared to the cross-flow instabilities. The growth rate of the BL instabilities is exponential, as shown on Fig. 6 and predicted by linear stability theory. In particular, Tollmien-Schlichting (TS) waves form before the boundary layer separates, and Kelvin-Helmholtz (KH) instabilities are ultimately responsible for transition after separation. Turbulence constitutes a new, "stable" flow regime that prevents instabilities to keep growing exponentially in space and time.

From a quantitative perspective, ILES and Vreman-LES also predict a similar evolution of the boundary layer before separation; which occurs at $x_s/c = 0.458$ and 0.466, respectively. The Vreman model, however, slightly underpredicts the growth rate of KH modes in the separated region, as shown in Fig. 6, and leads to delayed transition and reattachment compared to ILES and the experimental data. As a result, the displacement thickness and the shape parameter evolve differently after x_s/c, as illustrated in Fig. 5. While the ILES and Vreman-LES results are overall in good agreement, the small discrepancies in the shape parameter and the size of the separation bubble may have important consequences in practice and lead to inaccurate drag predictions.

In short, the numerical results for the Eppler 387 wing indicate that ILES is better suited than explicit LES to simulate transitional flows. This is justified by the following observation: While some dissipation is required to account for the unresolved scales in a turbulent flow, this is not the case along the laminar portion of the boundary layer in which the transition process takes place. As such, directly removing spurious diffusion coming from an SGS model, as in ILES, turns out to be a better approach.
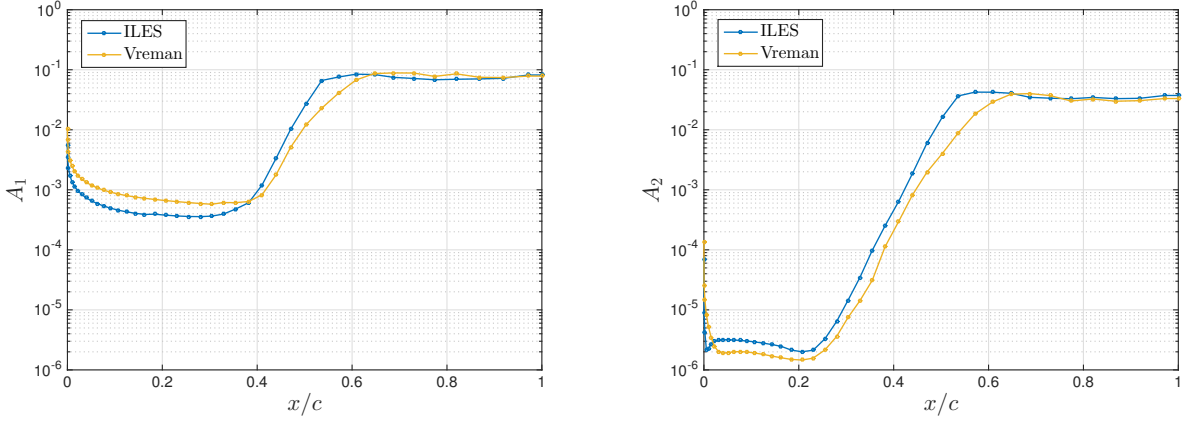
Figure 6: ILES and Vreman-LES predictions of the amplitude of streamwise (left) and cross-flow (right) instabilities along the suction side of the Eppler 387 wing.

VI.   The Taylor-Green vortex problem

A.   Case description

The Taylor-Green vortex[38] (TGV) is a canonical problem to study vortex dynamics, turbulence transition and turbulence decay. It contains several flow regimes in a single construct and is therefore an excellent test case for our purpose. In particular, the TGV problem describes the evolution of the flow in a cubic domain $\Omega = [-L\pi, L\pi)^3$ with triple periodic boundaries, starting from the smooth initial condition:

$$
\begin{aligned}
u &= U_0 \sin\left(\frac{x}{L}\right) \cos\left(\frac{y}{L}\right) \cos\left(\frac{z}{L}\right), \\
v &= -U_0 \cos\left(\frac{x}{L}\right) \sin\left(\frac{y}{L}\right) \cos\left(\frac{z}{L}\right), \\
w &= 0, \\
p &= p_0 + \frac{\rho U_0^2}{16} \left(\cos\left(\frac{2x}{L}\right) + \cos\left(\frac{2y}{L}\right) \right) \left(\cos\left(\frac{2z}{L}\right) + 2 \right), \\
T &= T_0.
\end{aligned}
\tag{19}
$$

The large-scale eddy in the initial condition (19) leads to smaller and smaller structures through vortex stretching. Near $t \approx 7\ L/U_0$, the vortical structures undergo structural changes, and around $t \approx 9\ L/U_0$ they break down and the flow transitions to turbulence. Since there is no external forcing to sustain turbulence, the smallest turbulent structures and thus the maximum dissipation rate of kinetic energy occur at this time. After $t \approx 9\ L/U_0$, the turbulent motion dissipates all the kinetic energy until the flow eventually comes to rest. This decay phase is similar to that in decaying homogeneous isotropic turbulence, yet not isotropic here.

In this paper, we consider the TGV problem at Reynolds number $Re = U_0 L/\nu = 1600$. In order to render the flow nearly incompressible and enable comparison with DNS data,[40] the Mach number is set to $M = U_0/a_0 = 0.1$, where a_0 denotes the speed of sound at the temperature T_0. Results for the effect of the Riemann solver, the SGS model and the time-step size are reported.

B.   Details of the numerical discretization

Third-order IEDG and DIRK(3,3) schemes are used for the spatial and temporal discretization, respectively. The computational domain is partitioned using a uniform linear grid with $64 \times 64 \times 64$ hexahedra; which corresponds to $128 \times 128 \times 128$ unique grid points (i.e. counting duplicated DG nodes only once) and $192 \times 192 \times 192$ total grid points (i.e. including duplication). The computation is performed from $t = 0$ to $t = 15\ L/U_0$ with a baseline time-step size $\Delta t = 3.682 \cdot 10^{-2}\ L/U_0$ corresponding to a CFL number $U_0\ \Delta t/\Delta x = 0.375$.

C. Effect of the Riemann solver

No explicit SGS model is used in this section in order to investigate the effect of the Riemann solver only. Since the main effect of the subgrid scales in a turbulent flow is dissipation, algorithms with small numerical dissipation have been argued to be preferred for LES. This way, it is only the SGS model that introduces dissipation and is responsible for replicating the effects of the sugbrid scale turbulence. This motivates us to investigate the Riemann solvers from the perspective of numerical dissipation. The methodology and nomenclature used for the analysis is presented in Appendix C. Due to the symmetries in the incompressible Navier-Stokes equations, the convective and viscous operators preserve and dissipate kinetic energy, respectively. For this reason, the numerical dissipation in incompressible solvers is usually defined in terms of kinetic energy. In the compressible setting, however, it is entropy, instead of kinetic energy, that is preserved and generated by the convective and viscous operators, respectively; and it is only in the low Mach number limit that conservation of entropy leads to conservation of kinetic energy.

Figure 7 shows the time evolution of kinetic energy dissipation rate $-dE_k/dt$ (left) and entropy-based numerical dissipation Π_S (right) for the three stabilization matrices considered. From these figures, the following remarks follow. First, despite under-resolution, no major differences are observed between Riemann solvers. Second, numerical dissipation is an increasing function of the kinetic energy contained in the subgrid scales. This shows that DG methods have a built-in implicit LES capability: Inter-element jumps act as a self-stabilization mechanism and account for the effect of the subgrid scales in a similar manner as explicit SGS models do. Third, all Riemann solvers slightly underestimate the peak dissipation with respect to the DNS data.[40] Thus, the numerical dissipation is smaller than the true SGS dissipation (only) when the smallest turbulent structures appear. In particular, the numerical dissipation of kinetic energy is $\Pi_{E_k}^i \approx 1.6 \cdot 10^{-3}\ \rho_0 U_0^3 L^2$ at $t = 8.50\ L/U_0$; which is about $10^{-3}\ \rho_0 U_0^3 L^2$ smaller than necessary to match the DNS data. (Only) under these conditions, ILES may need to be further equipped with an explicit SGS model.

Table 3 collects the average absolute-value jump across elements on the periodic plane $x = -L\pi$, defined as

$$\frac{\int_{\mathcal{E}_h^I} |[\![\boldsymbol{u}_{h,j}]\!]|}{\int_{\mathcal{E}_h^I} |\langle \boldsymbol{u}_{h,j} \rangle|},$$

for each conserved quantity $j = 1, ..., 5$ at time $t = 8.50\ L/U_0$. Here, $[\![\boldsymbol{u}_{h,j}]\!] = \boldsymbol{u}_{h,j}^+ - \boldsymbol{u}_{h,j}^-$ and $\langle \boldsymbol{u}_{h,j} \rangle = (\boldsymbol{u}_{h,j}^+ + \boldsymbol{u}_{h,j}^-)/2$ denote the face jump and face average operators, respectively, and $\mathcal{E}_h^I$ is the set of interior faces, as described in Appendix A. Again, inter-element jumps act as a self-stabilization mechanism and provide an implicit LES capability. From this table, the stabilization matrix $\sigma = \lambda_{max}$ yields much smaller jumps in the momentum fields than the other two stabilization matrices. This is due to the over-upwinding for the momentum equations in this Riemann flux and shows that DG methods have an auto-correction mechanism (namely, adjusting the magnitude of the inter-element jumps, that is, the Riemann problem itself) to compensate for overshoots in the Riemann solver.
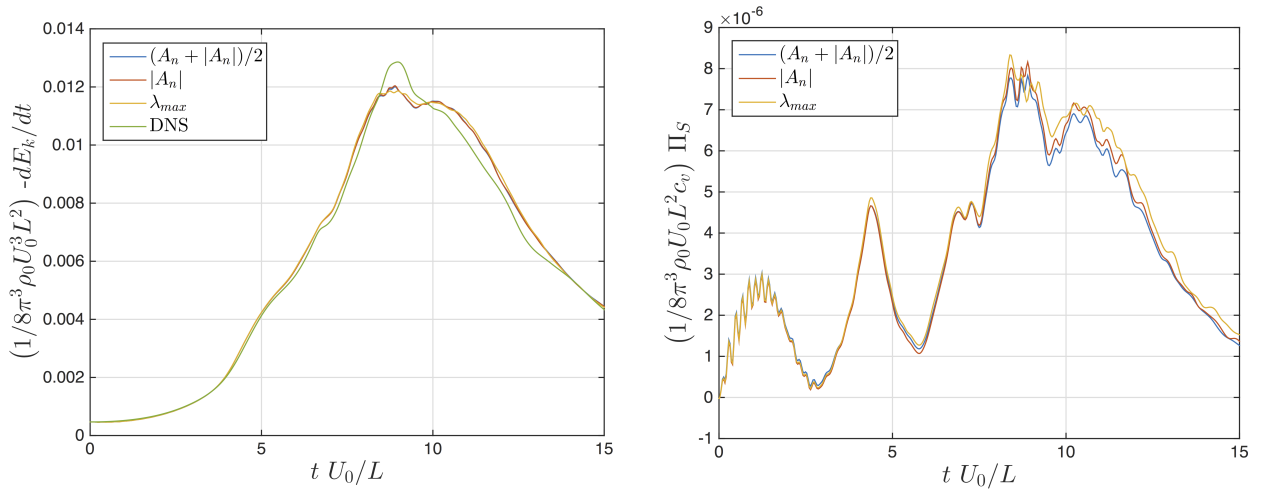

Figure 7: Time evolution of kinetic energy dissipation rate (left) and entropy-based numerical dissipation (right) for the Riemann solvers considered.
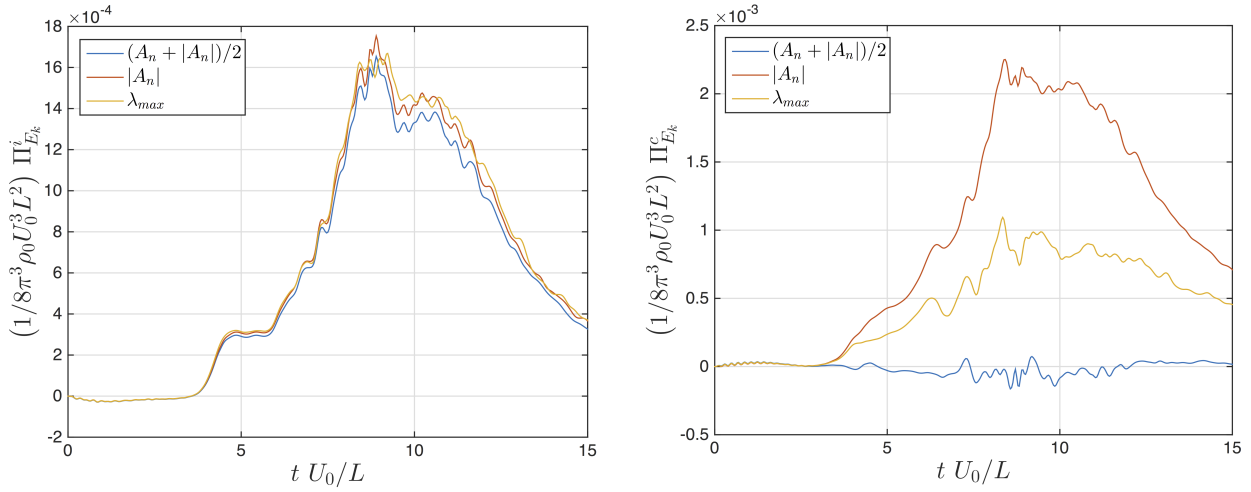
Figure 8: Numerical dissipation as computed from the incompressible (left) and compressible (right) kinetic energy equations.

Finally, Figure 8 shows the kinetic-energy-based numerical dissipation $\Pi^i_{E_k}$ and $\Pi^c_{E_k}$, defined from the incompressible and compressible kinetic energy equations, respectively. From this figure, $\Pi^c_{E_k}$ may yield fallacious results even at this low Mach number, and it is the incompressible kinetic energy equation that provides a more realistic description of the true numerical dissipation. From a theoretical perspective, this is attributed to the fact that it is the symmetries in the incompressible kinetic energy equation that are closer to remain in the compressible setting. Also, numerical dissipation of kinetic energy is only non-zero after (dynamic) subgrid-scale structures appear in the flow at $t \approx 4\ L/U_0$. Unlike explicit SGS models in the section below, the built-in implicit LES capability in DG methods succeeds to detect the presence of subgrid scales and add numerical dissipation only under those conditions. The non-zero numerical entropy generation Π_S at $t < 3\ L/U_0$ in Figure 7 is due subgrid-scale acoustic modes.

D. Effect of the SGS model

Figure 9 shows the dissipation rate of kinetic energy predicted by ILES, Smagorinky-LES, WALE-LES and Vreman-LES. The stabilization matrix is $\sigma = (A_n + |A_n|)/2$ in all cases. The three SGS models fail to vanish in the laminar

	ρ	ρv_1	ρv_2	ρv_3	ρE
		Study of Riemann solver			
$(A_n + |A_n|)/2$	8.8654E − 5	3.2592E − 1	3.3158E − 3	6.2183E − 3	1.1643E − 4
$|A_n|$	8.7554E − 5	4.4186E − 1	2.9354E − 3	5.3456E − 3	1.1563E − 4
λ_{max}	9.0452E − 5	1.5166E − 1	9.0681E − 4	1.6674E − 3	1.2649E − 4
		Study of SGS model			
ILES	8.8654E − 5	3.2592E − 1	3.3158E − 3	6.2183E − 3	1.1643E − 4
Smagorinsky-LES	4.7599E − 5	1.8550E − 1	1.8706E − 3	3.3527E − 3	6.2188E − 5
Vreman-LES	4.9323E − 5	5.2481E − 2	2.0054E − 3	3.5868E − 3	6.4739E − 5
		Study of time-step size			
CFL = 1.5000	8.4671E − 5	3.6338E − 1	3.2513E − 3	6.6477E − 3	1.1061E − 4
CFL = 0.7500	8.7919E − 5	9.3606E − 2	3.3199E − 3	6.1912E − 3	1.1541E − 4
CFL = 0.3750	8.8654E − 5	3.2592E − 1	3.3158E − 3	6.2183E − 3	1.1643E − 4
CFL = 0.1875	8.7530E − 5	1.1877E − 1	3.3171E − 3	6.1517E − 3	1.1483E − 4

Table 3: Average absolute-value jump across elements on the periodic plane $x = -L\pi$ of the Taylor-Green vortex at $t = 8.50\ L/U_0$.
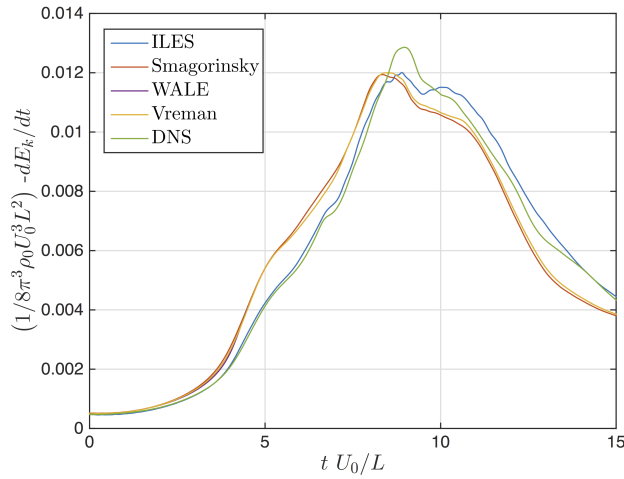
Figure 9: Time evolution of dissipation rate of kinetic energy in ILES, Smagorinsky-LES, WALE-LES and Vreman-LES.

regime, i.e. before $t < 7 \sim 9 \ L/U_0$, and produce unphysical dissipation during this phase. This shows again the limitations of explicit SGS modeling to simulate transitional flows. As in the Eppler 387 wing, the built-in self-stabilization in DG methods provides a more accurate mechanism to detect the presence of SGS scales and add numerical dissipation only under those conditions than any of the SGS models considered. Also, Table 3 collects the average absolute-value jump across elements and Figure 10 shows a snapshot of the vorticity norm on the periodic plane $x = -L\pi$ at $t = 8 \ L/U_0$ for ILES (left), Smagorinsky-LES (center) and Vreman-LES (right). While the jumps in the numerical solution are smaller and the vorticity norm field is smoother with an SGS model due to the non-zero eddy viscosity, ILES actually provides a more accurate representation of the flowfield.

The larger dissipation in explicit LES at short times corresponds to effectively solving a smaller Reynolds number flow. The maximum dissipation rate actually occurs at an earlier time compared to DNS data;[40] which is characteristic of the Taylor-Green vortex at lower Reynolds numbers.[5] WALE-LES again failed to converge at $t \approx 4.59 \ L/U_0$. This lack of robustness limits the practical applicability of this model for high-order LES with implicit time integrators. Unlike for wall-bounded flows, such as in the Eppler wing in Section V and the turbulent channel flow in Section VII, no major differences are observed between the Smagorinsky and the Vreman SGS models here. As expected, this points directly to the incapability of the Smagorinsky model to vanish near the wall as one the main limitation of this model. Due to the unphysical dissipation of explicit LES at short times, the spectral distribution of kinetic energy evolves differently compared to that in ILES and DNS, and no meaningful conclusions can be inferred on the performance of the SGS models in the turbulent regime.
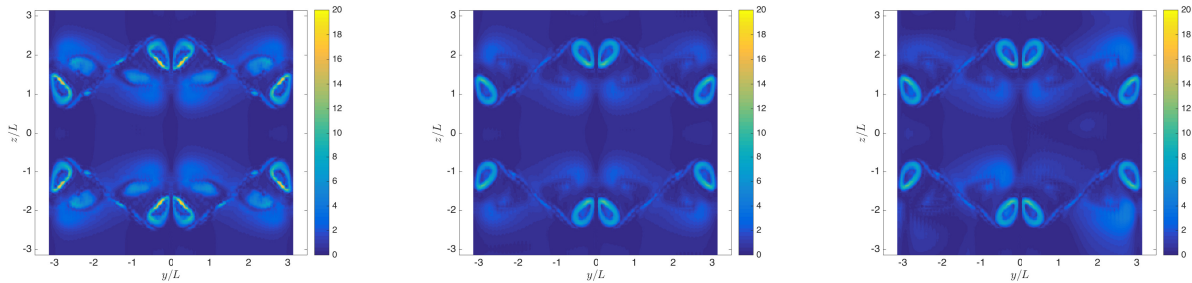

Figure 10: Snapshot of vorticity norm $|\boldsymbol{\omega}| \ L/U_0$ on the periodic plane $x = -L\pi$ at $t = 8 \ L/U_0$ for ILES (left), Smagorinsky-LES (center) and Vreman-LES (right). WALE-LES leaded to nonlinear instability and the breakdown of the iterative solver at $t \ U_0/L \approx 4.59$.

American Institute of Aeronautics and Astronautics

E. Effect of the time resolution

We consider the time-step sizes $\Delta t = (14.7262, 7.3631, 3.6816, 1.8408) \cdot 10^{-2} \ L/U_0$; which correspond to CFL numbers $U_0 \, \Delta t / \Delta x = 1.50, 0.75, 0.375,$ and 0.1875, respectively. ILES with $\sigma = (A_n + |A_n|)/2$ is used in all cases. Figure 11 shows the time evolution of kinetic energy dissipation rate (left) and entropy-based numerical dissipation (right) for these time-step sizes. Both $-dE_k/dt$ and Π_S converge to an asymptotic solution as the time step is refined; which corresponds to the continuous-in-time solution of the semi-discrete system in Eq. (4). From this figure, minor differences are observed for the four time steps considered. This is due to the fact that the vorticity and entropy modes that are captured by (4) can be accurately resolved with CFL $\lesssim 1$, and these are the most important features in the dynamics of low Mach number turbulent flows. Further refining in time below CFL ~ 1 allows to resolve acoustics modes as well, as illustrated in Fig. 11 through the oscillations in Π_S. These oscillations correspond to pressure waves and are particularly intense at early times due to the acoustic imbalance in the initial condition.

We note that the space discretization error (responsible for the mismatch between the CFL = 0.1875 case and the DNS data) vastly dominates the time discretization error even at CFL = 1.50. Optimal LES implementations, in which space and time discretization errors are properly balanced, may therefore be achieved with local CFL numbers significantly larger than one. In addition, the asymptotic solution as the time step is refined $\Delta t \downarrow 0$ in wall-bounded flows could be achieved with much larger global CFL numbers than in the TGV problem, since the smallest element size is usually located in a laminar region of the flow, e.g. in the viscous sublayer or near the leading edge before the flow transitions to turbulence. This shows promise for implicit time integration in high-order DG-based LES due to the severe CFL restrictions of explicit schemes in the high-order setting.
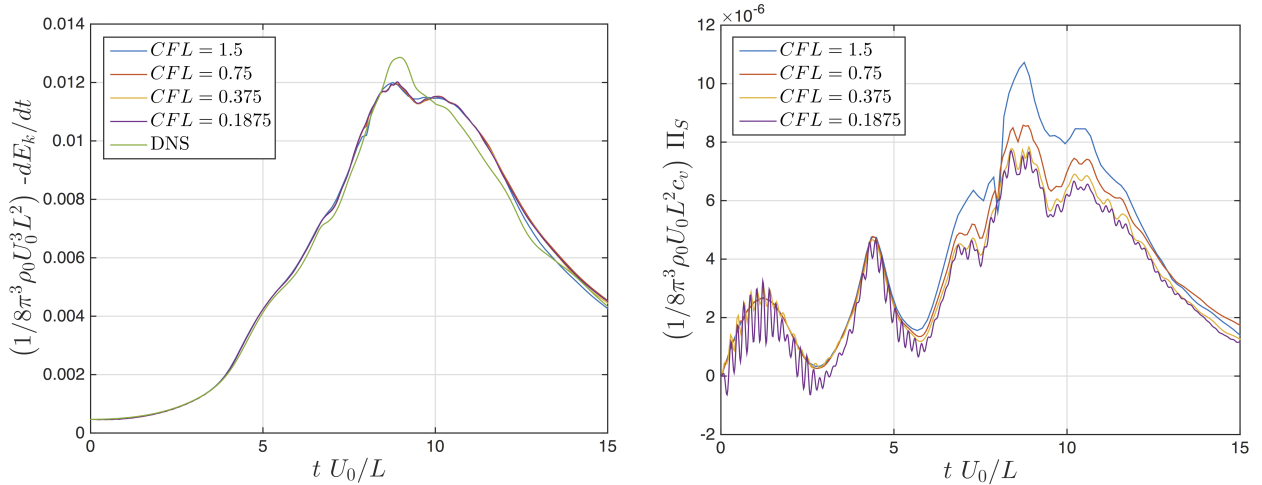

Figure 11: Time evolution of kinetic energy dissipation rate (left) and entropy-based numerical dissipation (right) for the time-step sizes considered.

VII. Turbulent channel flow

A. Case description

Finally, we investigate the performance of the LES approaches for wall-bounded turbulence. Results for the effect of the Riemann solver, SGS model and accuracy order are reported. To this end, we consider the turbulent channel flow[20] at $Re_\tau = 182$ and 544, where $Re_\tau = u_\tau \delta / \nu$ denotes the Reynolds number based on the friction velocity $u_\tau = \sqrt{\tau_w/\rho}$ and the channel half-width δ. The bulk Mach number is $M_b = u_b/a = 0.2$, where $u_b = \int_0^{2\delta} u(y) \, dy \ / \ 2\delta$ is the bulk velocity and a is the speed of sound. A homogeneous, time-dependent volumetric force is imposed in the streamwise direction to compensate the friction at the walls and ensure the mass flow remains constant in the channel. In particular, the mass flow is that required to achieve the desired Re_τ according to DNS results.[20] As a consequence, the Re_τ computed in LES (denoted by Re_τ^{LES} hereinafter) may not agree with the target Re_τ (denoted by Re_τ^{target}) if the resolution is not sufficiently fine. This will be shown to be the case at $Re_\tau^{target} = 544$.

B. Details of the numerical discretization

Third-order IEDG and DIRK(3,3) schemes are used for the baseline spatial and temporal discretization, respectively. The channel size is $4\pi\delta \times 2\delta \times 2\pi\delta$ and the number of elements $48 \times 32 \times 40$ (i.e. $144 \times 96 \times 120$ unique grid points) in the streamwise, wall-normal and spanwise directions, respectively. The same mesh is used for both Reynolds numbers in order to obtain different resolutions in wall units and provide insight on the mesh requirements to resolve wall-bounded turbulent flows. The velocity, length and time scales for wall unit non-dimensionalization are u_τ, ν/u_τ and ν/u_τ^2, respectively. The average spacing between high-order nodes $(\Delta x_{avg}^+, \Delta y_{avg}^+, \Delta z_{avg}^+)$, near-wall resolution Δy_w^+ and time-step size Δt^+ are summarized in Table 4. The high-order nodes in the wall-normal direction y are distributed uniformly in a mapped coordinate ξ that is related to y through

$$\frac{y}{\delta} = \frac{\sin(\xi\pi/2)}{\sin(\pi/2)} + 1, \quad -1 \leq \xi \leq 1.$$

A run-up time $t_1^+ = 2000$ is used to ensure the flow achieves its steady-state distribution on the chaotic attractor. Then, the statistics are collected over a time span of $t_2^+ = 1000$ to ensure the statistical convergence of the mean velocity and Reynolds stresses across the channel.

	$Re_\tau^{target} = 182$	$Re_\tau^{target} = 544$
Δx_{avg}^+	23.8	71.2
Δy_{avg}^+	5.69	17.0
Δz_{avg}^+	14.3	42.7
Δy_w^+	0.44	1.31
Δt^+	0.29	0.74

Table 4: Average spacing between high-order nodes, near-wall resolution and time-step size for LES of turbulent channel flow.

C. Effect of the Riemann solver

Figure 12 shows the mean velocity profile at $Re_\tau^{target} = 182$ and 544 for the three stabilization matrices considered. The predicted values of Re_τ^{LES} are collected in Table 5. Since no significant differences are observed between the three stabilization matrices in terms of wall friction, mean velocity and Reynolds stresses, the analysis of the ILES results is deferred to the comparison between ILES and explicit SGS models below.
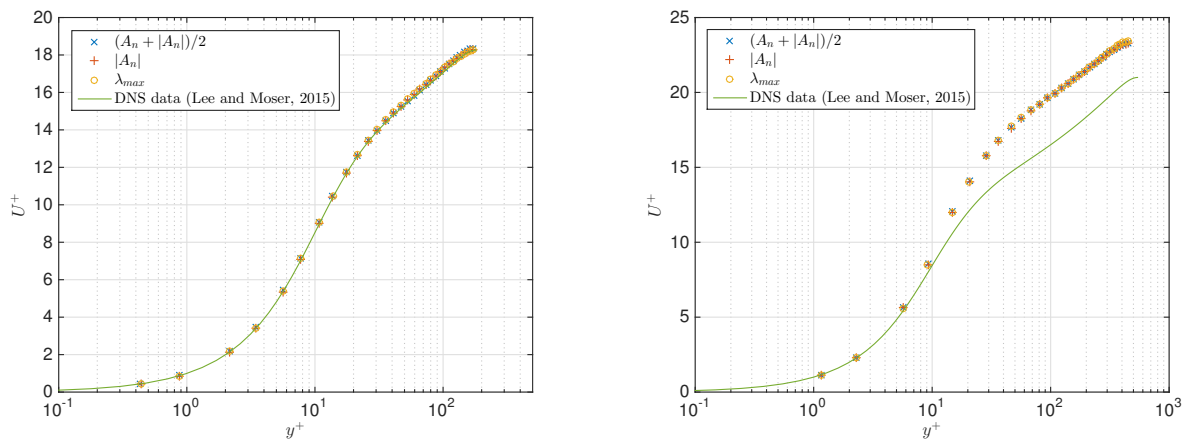

Figure 12: ILES predictions of mean velocity profile for channel flow at $Re_\tau^{target} = 182$ (left) and 544 (right). Re_τ^{LES} is used for non-dimensionalization.

	$Re_\tau^{target} = 182$	$Re_\tau^{target} = 544$
Study of Riemann solver		
$(A_n + |A_n|)/2$	180.8	478.7
$|A_n|$	181.0	479.1
λ_{max}	181.1	477.7
Study of SGS model		
ILES	180.8	478.7
Smagorinsky-LES	191.5	658.1
WALE-LES	173.3	452.6
Vreman-LES	170.1	468.4
Study of accuracy order		
Third-order	180.8	478.7
Fifth-order	–	523.9

Table 5: Values of Re_τ^{LES} computed in LES.

D. Effect of the SGS model

Figures 13 and 14 show the mean velocity profile at $Re_\tau^{target} = 182$ and 544, respectively, for ILES, Smagorinsky-LES, WALE-LES and Vreman-LES. The stabilization matrix is $\sigma = (A_n + |A_n|)/2$ in all cases. Two different types of non-dimensionalization are used on the left and right images of these figures. On the left images, the velocity and length scales at the wall are computed from τ_w^{LES}. This will be the adequate non-dimensionalization to investigate if the viscous and log layers are properly resolved, as we shall see below. On the right images, the target τ_w is used for non-dimensionalization. This way, the data from the different simulations are non-dimensionalized with respect to the same reference quantities, so that the scaling factor between dimensional and non-dimensional data is the same in all cases. As a result, the dimensional velocity profiles can be directly compared from these figures. This type of non-dimensionalization will be useful to understand the reasons for the mismatch between LES and DNS. Also, Figure 15 shows the Reynolds stresses at $Re_\tau^{target} = 182$ and Table 5 collects the predicted values of Re_τ^{LES}. The results in these figures can be interpreted as follows:

Viscous sublayer ($y^+ \lesssim 10$)**:** Theoretical results show that $\tau_{xy}(y) \approx \tau_w$ and that molecular transport dominates over turbulent transport in this region. This yields the well-known result $U^+ = y^+$. From the left images in Figures 13 and 14, the viscous sublayer is accurately resolved at both Reynolds numbers by ILES, WALE-LES and Vreman-LES. Provided enough resolution is available to capture the mean flow and no eddy viscosity is added by the SGS model (if
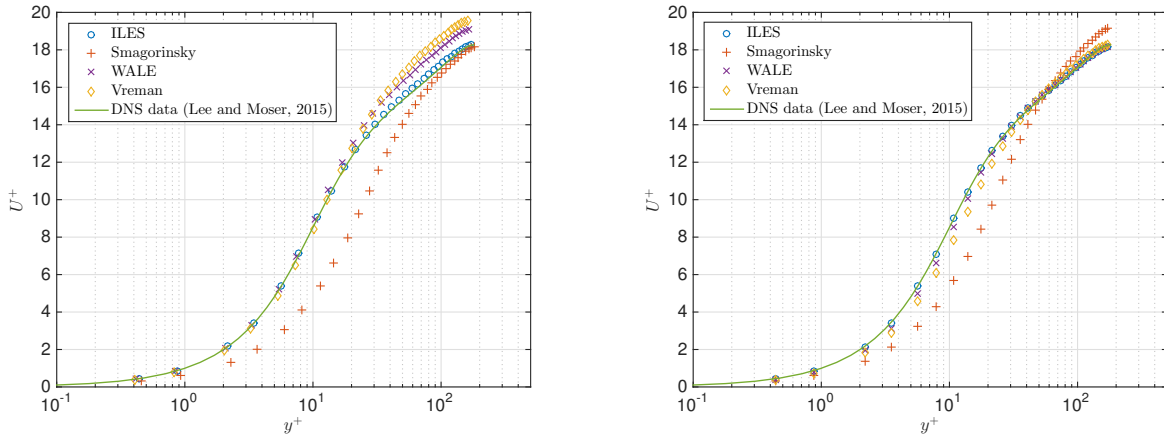

Figure 13: ILES and explicit LES predictions of mean velocity profile for channel flow at $Re_\tau^{target} = 182$. Re_τ^{LES} and Re_τ^{target} are used for non-dimensionalization on the left and right images, respectively.
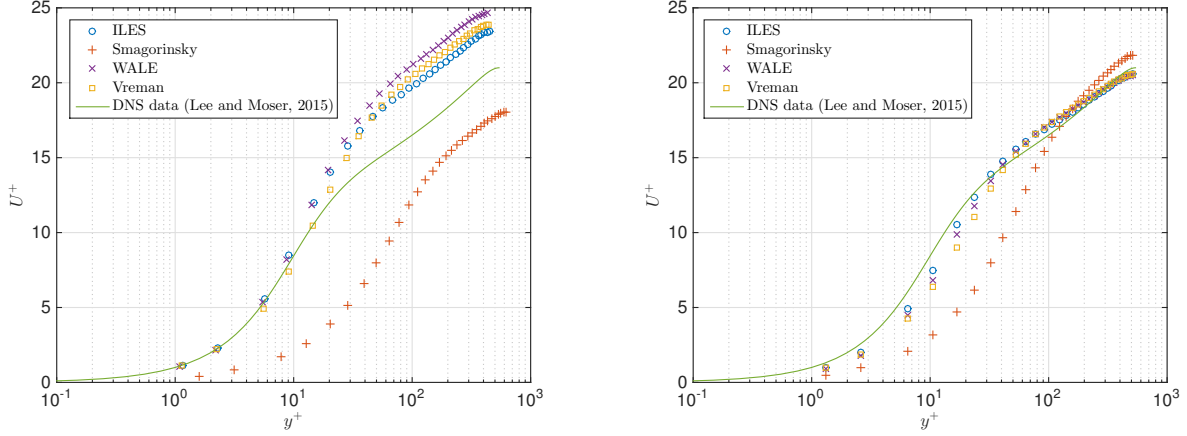
Figure 14: ILES and explicit LES predictions of mean velocity profile for channel flow at $Re_\tau^{target} = 544$. Re_τ^{LES} and Re_τ^{target} are used for non-dimensionalization on the left and right images, respectively.

any), this is expected due to the laminar nature of the flow in this region. However, as in the Eppler 387 wing, the eddy viscosity fails to vanish near the wall in Smagorisnky-LES and this leads to inaccurate skin friction and mean velocity predictions, even at the low $Re_\tau^{target} = 182$. In particular, the average eddy viscosity at the wall in Smagorinsky-LES is $\nu_e^S|_w = 0.934\,\nu$ and $0.248\,\nu$ at $Re_\tau^{target} = 182$ and 544, respectively.

Log layer ($y^+ \gtrsim 40$): In this layer, $\tau_{xy}(y) \approx \tau_w$ and turbulent transport dominates over molecular transport. This, combined with the mixing-length hypothesis $\ell = \kappa\, d_w$, where ℓ is the mixing length, κ is the von Kármán constant and d_w is the distance to the wall, leads to $U^+ = (1/\kappa)\log y^+ + B$. DNS data[20] suggest $\kappa = 0.384 \pm 0.004$ and $B = 4.27$. The left images in Figures 13 and 14 show that all simulations succeed to predict this logarithmic dependence with the correct mixing length $\ell = \kappa_{LES}\, d_w$, where $\kappa_{LES} \approx 0.38$. The matching velocity between the buffer and log layers, however, does not agree in general with the DNS data. This implies that $B_{LES} \neq 4.27$ and is likely due to insufficient resolution in the buffer layer and, to a lessen extent, in the log layer. The incorrect outer velocity seen by the viscous sublayer is responsible for the misprediction of the wall shear stress in Table 5.

Buffer layer ($10 \lesssim y^+ \lesssim 40$): At $Re_\tau^{target} = 182$, the buffer layer is only properly resolved by ILES. At $Re_\tau^{target} = 544$, none of the simulations succeeds to resolve this layer with the available resolution. ILES, however, is again closer to the DNS data than any of the simulations with an explicit SGS model. We note that all the simulations *over-transport* momentum in the buffer layer and therefore d^2u/dy^2 is less negative than the true value to compensate, as illustrated in Figure 14. This yields a larger velocity at the end of the buffer layer, and translates into LES underpredicting the skin friction at the wall for a given mass flow. Hence, the velocity jump across the buffer layer is an increasing function of momentum transport, either numerical or from an SGS model; which is consistent with Figures 9 and 11 in.[26] We note that, while *over-transportive*, the turbulent kinetic energy in LES is larger than in DNS (see Fig. 15). This indicates that the dissipation of resolved kinetic energy due to numerical and SGS modeled viscosity is smaller than the actual subgrid scale dissipation. A ratio *momentum transport-to-dissipation* larger than the true SGS value is postulated to be due to the different time scales of the resolved and unresolved fields. In particular, transport and dissipation depend differently on the time scales of the SGS stress tensor. This illustrates some challenges to accurately model SGS transport and dissipation simultaneously if the time scales in τ^{SGS} –either from an SGS model or from the discretization error– are those of the largest resolved scales.

E. Effect of the accuracy order

For a fixed number of degrees of freedom, high-order methods are known to outperform low-order methods in terms of accuracy in well-resolved simulations, such as DNS of turbulent flows, due to their faster convergence rate as the element size tends to zero. In the case of under-resolved simulations, such as (by definition) in LES, the order of convergence loses relevance, and it is the dissipative and dispersive errors for under-resolved wavelengths that dominate the approximation quality.[24, 25] Whether improved predictability is also achieved for under-resolved turbulence simulations is therefore less clear. In order to gain insight into this question, we consider a fifth-order ILES discretization of the channel flow at $Re_\tau^{target} = 544$. The DOF count and time-step size are the same as those in the
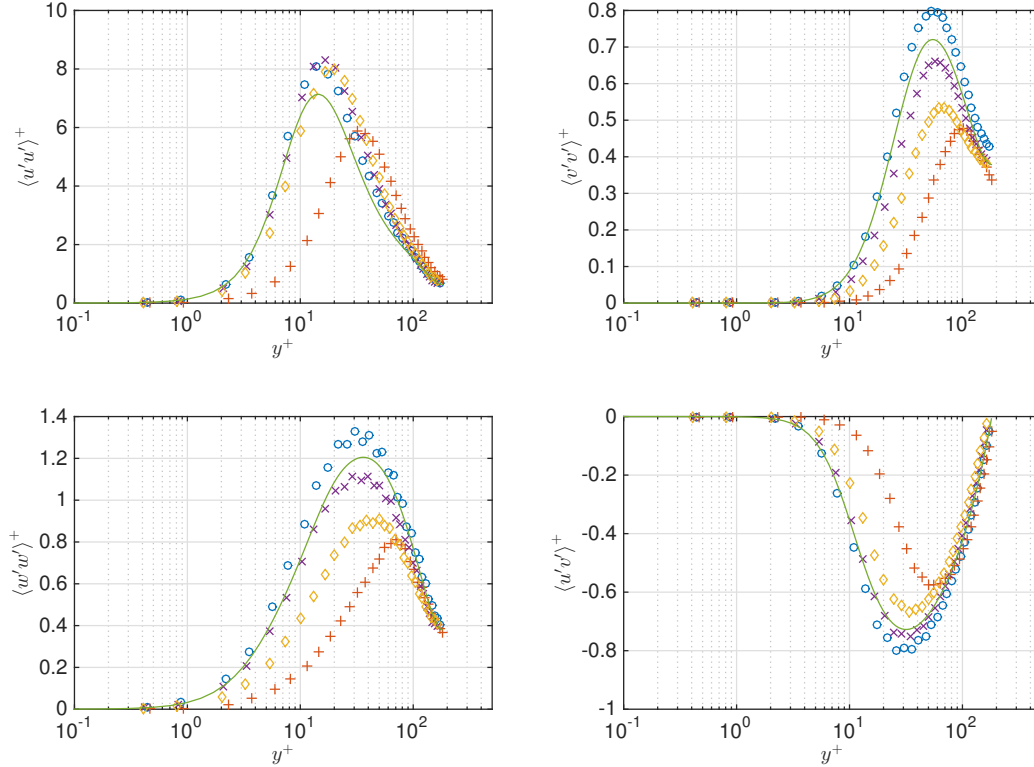
Figure 15: ILES and explicit LES predictions of Reynolds stresses for channel flow at $Re_\tau^{target} = 182$. Re_τ^{LES} is used for non-dimensionalization. The color legend is shown in Figures 13 and 14.

previous sections, and the stabilization matrix is set to $\sigma = (A_n + |A_n|)/2$.

Despite under-resolution, the fifth-order discretization provides a more accurate description of the mean flow, as shown in Fig. 16, as well as of the Reynolds stresses (not shown here). Also, $Re_\tau^{LES} = 523.9$ for fifth-order ILES, as opposed to $Re_\tau^{LES} = 478.7$ in the third-order solution. The improved performance of the fifth-order scheme is justified as follows: Accurately resolving as many of the scales that can be theoretically captured with the available resolution (Shannon theorem) plays a more important role for these flow conditions than that of the subgrid scales, and this is better achieved with the fifth-order discretization. Whether this also holds as the range of subgrid scales increases, that is, for larger Reynolds number flows, is the subject of ongoing research.

VIII. Conclusions

We investigated the relation between numerical discretization, subgrid-scale modeling and the resulting LES solver in the framework of high-order DG methods. The role of the Riemann solver, SGS model, time resolution, and accuracy order were examined for a variety of flow regimes, including transition to turbulence, wall-free turbulence, wall-bounded turbulence, and turbulence decay. The transitional flow over the Eppler 387 wing, the Taylor-Green vortex problem and the turbulent channel flow were considered to this end. The main findings and contributions of this paper are summarized as follows:

- **Theoretical contributions:** We derived the connection between the stabilization matrix in hybridized DG methods and the resulting Riemann solver; which is important to accurately resolve high Reynolds number turbulent flows. Also, we presented an entropy stability analysis for hybridized DG methods. The analogies in the entropy equalities for hybridized and standard DG methods imply that most well-known results on DG and Riemann solvers carry over to the hybridized framework.
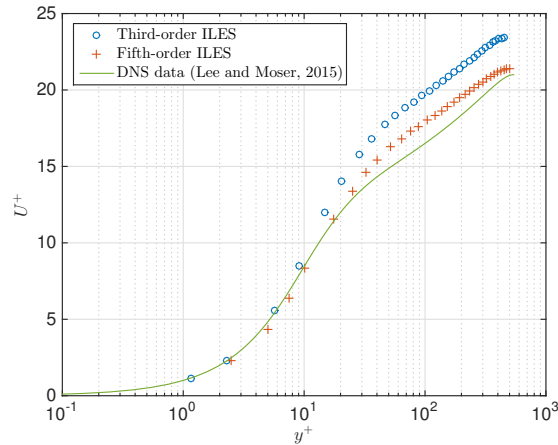
Figure 16: Third- and fifth-order ILES predictions of mean velocity profile for channel flow at $Re_\tau^{target} = 544$. Re_τ^{LES} is used for non-dimensionalization.

- **Suitability of high-order DG methods for LES:** The number of degrees of freedom to accurately resolve transition from laminar to turbulent regime can be significantly reduced by using a high-order approach. In particular, simulating transitional flows is challenging mostly due to the small magnitude of the instabilities involved, rather than their length and time scales. Hence, low-order schemes may kill the small instabilities because of high numerical dissipation even when the mesh size and time-step size are sufficiently small to represent the length and time scales of the instabilities.

  The LES predictions of the turbulent channel flow also significantly improved by increasing the accuracy order of the discretization scheme. This illustrates that accurately resolving the large scales in a turbulent flow by using a high-order method may play a more important role than that of the subgrid scales.

  Finally, numerical results showed that DG methods have a built-in implicit LES capability and add numerical dissipation in under-resolved turbulence simulations. This is supported by the theoretical results in Section III.

- **Role of the Riemann solver in DG-based LES:** No significant differences were observed between Riemann solvers for transition prediction, wall-free turbulence, wall-bounded turbulence and turbulence decay, even in the presence of significant under-resolution. Numerical results showed that DG methods have an auto-correction mechanism to partially compensate for overshoots in the Riemann solver (namely, adjusting the magnitude of the inter-element jumps as necessary); which justifies this observation.

- **Implicit vs. explicit subgrid-scale modeling:** First, implicit LES is better suited than explicit SGS modeling for transitional flows. In particular, the built-in implicit LES capability in DG methods provides a more accurate mechanism to detect the presence of subgrid scales and add numerical dissipation only under those conditions than explicit SGS models. Second, implicit LES was also shown to outperform explicit models for the wall-free and wall-bounded turbulent flows considered. Whether this continues to hold as the range of subgrid scales increases, i.e. for larger Reynolds number flows, is the subject of ongoing research. Third, the ratio *momentum transport-to-dissipation* due to discretization errors and explicit SGS models were shown to be larger than the true SGS value; which is attributed to the different time scales in the resolved and unresolved turbulent fields. This illustrates the challenges to accurately model subgrid-scale transport and dissipation simultaneously if the time scales in τ^{SGS} –either from an SGS model or from the discretization error– are those of the largest resolved scales.

- **Role of the time-step size:** Optimal LES implementations, in which space and time discretization errors are properly balanced, may be achieved with local CFL numbers significantly larger than one. For wall-bounded turbulent flows, this may result in a global CFL number much larger than one and shows promise for implicit time integration for high-order DG-based LES.

American Institute of Aeronautics and Astronautics

Acknowledgments

A.   Notation used for the hybridized DG discretization

Finite element mesh

Let $\Omega \subseteq \mathbb{R}^d$ with $d = 3$ be a bounded physical domain with Lipschitz boundary $\partial\Omega$. We denote by $\mathcal{T}_h$ a collection of disjoint, regular, p-th degree curved elements K that partition Ω, and set $\partial\mathcal{T}_h := \{\partial K : K \in \mathcal{T}_h\}$ to be the collection of the boundaries of the elements in $\mathcal{T}_h$. For an element K of the collection $\mathcal{T}_h$, $F = \partial K \cap \partial\Omega$ is a boundary face if its $d - 1$ Lebesgue measure is nonzero. For two elements K^+ and K^- of $\mathcal{T}_h$, $F = \partial K^+ \cap \partial K^-$ is the interior face between K^+ and K^- if its $d - 1$ Lebesgue measure is nonzero. We denote by $\mathcal{E}_h^I$ and $\mathcal{E}_h^B$ the set of interior and boundary faces, respectively, and we define $\mathcal{E}_h := \mathcal{E}_h^I \cup \mathcal{E}_h^B$ as the union of interior and boundary faces. $\partial\mathcal{T}_h^B$ and $\partial\mathcal{T}_h^I$ are defined in an analogous manner. Note that, by definition, $\partial\mathcal{T}_h$ and $\mathcal{E}_h$ are different. More precisely, an interior face is counted twice in $\partial\mathcal{T}_h$ but only once in $\mathcal{E}_h$, whereas a boundary face is counted once both in $\partial\mathcal{T}_h$ and $\mathcal{E}_h$.

Finite element spaces

Let $\mathcal{P}_k(D)$ denote the space of real polynomials of degree k on some Lebesgue measurable set $D \subset \mathbb{R}^n$, let $L^2(D)$ be the space of Lebesgue square-integrable functions on D, and let ψ_K^p denote the p-th degree parametric mapping from the reference element K_{ref} to some element $K \in \mathcal{T}_h$ in the physical domain. We then introduce the following discontinuous finite element spaces:

$$\mathcal{Q}_h^k = \left\{ \boldsymbol{r}_h \in [L^2(\mathcal{T}_h)]^{m \times d} \ : \ (\boldsymbol{r}_h \circ \psi_K^p)|_K \in [\mathcal{P}_k(K_{ref})]^{m \times d} \ \forall K \in \mathcal{T}_h \right\}, \tag{20a}$$

$$\mathcal{V}_h^k = \left\{ \boldsymbol{w}_h \in [L^2(\mathcal{T}_h)]^m \ : \ (\boldsymbol{w}_h \circ \psi_K^p)|_K \in [\mathcal{P}_k(K_{ref})]^m \ \forall K \in \mathcal{T}_h \right\}, \tag{20b}$$

where m denotes the number of equations of the conservation law, i.e. $m = d + 2$ for the Navier-Stokes system. In addition, let us denote the p-th degree parametric mapping from the reference face F_{ref} to some physical face F by ϕ_F^p. We then introduce the following traced finite element space on the mesh skeleton $\mathcal{E}_h$:

$$\mathcal{M}_h^k = \left\{ \boldsymbol{\mu}_h \in [L^2(\mathcal{E}_h)]^m \ : \ (\boldsymbol{\mu}_h \circ \phi_F^p)|_F \in [\mathcal{P}^k(F_{ref})]^m \ \forall F \in \mathcal{E}_h, \ \text{and} \ \boldsymbol{\mu}_h|_{\mathcal{E}_h^E} \in [C^0(\mathcal{E}_h^E)]^m \right\}, \tag{21}$$

where $\mathcal{E}_h^E$ is a subset of $\mathcal{E}_h$. Note that $\mathcal{M}_h^k$ consists of functions which are continuous on $\mathcal{E}_h^E$ and discontinuous on $\mathcal{E}_h^H := \mathcal{E}_h \backslash \mathcal{E}_h^E$. Different choices of $\mathcal{E}_h^E$ lead to different discretization methods that have different properties in terms of accuracy, stability, and number of globally coupled unknowns.[11] In particular, the HDG, EDG and IEDG methods are obtained by setting $\mathcal{E}_h^E = \emptyset$, $\mathcal{E}_h^E = \mathcal{E}_h$ and $\mathcal{E}_h^E = \mathcal{E}_h^I$, respectively.

We finally define several inner products associated with these finite element spaces. In particular, given $\boldsymbol{w}_h, \boldsymbol{v}_h \in \mathcal{V}_h^k$, $\boldsymbol{W}_h, \boldsymbol{V}_h \in \mathcal{Q}_h^k$ and $\boldsymbol{\eta}_h, \boldsymbol{\zeta}_h \in \mathcal{M}_h^k$, we write

$$(\boldsymbol{w}_h, \boldsymbol{v}_h)_{\mathcal{T}_h} = \sum_{K \in \mathcal{T}_h} (\boldsymbol{w}_h, \boldsymbol{v}_h)_K = \sum_{K \in \mathcal{T}_h} \int_K \boldsymbol{w}_h \cdot \boldsymbol{v}_h, \tag{22a}$$

$$(\boldsymbol{W}_h, \boldsymbol{V}_h)_{\mathcal{T}_h} = \sum_{K \in \mathcal{T}_h} (\boldsymbol{W}_h, \boldsymbol{V}_h)_K = \sum_{K \in \mathcal{T}_h} \int_K \boldsymbol{W}_h : \boldsymbol{V}_h, \tag{22b}$$

$$\langle \boldsymbol{\eta}_h, \boldsymbol{\zeta}_h \rangle_{\partial\mathcal{T}_h} = \sum_{K \in \mathcal{T}_h} \langle \boldsymbol{\eta}_h, \boldsymbol{\zeta}_h \rangle_{\partial K} = \sum_{K \in \mathcal{T}_h} \int_{\partial K} \boldsymbol{\eta}_h \cdot \boldsymbol{\zeta}_h, \tag{22c}$$

where : denotes the Frobenius inner product.

B.   Boundary layer post-processing for the Eppler 387 wing

This appendix introduces the nomenclature and methodology used for the boundary layer (BL) post-processing in Section V. The BL analysis is based on the pseudo-velocity

$$\boldsymbol{v}^*(\boldsymbol{s}, n) := \int_0^n (\boldsymbol{\omega} \times \hat{\boldsymbol{n}}) \, dn', \tag{23}$$

where $\boldsymbol{\omega}$ denotes vorticity, and $(\boldsymbol{s}, n)$ is the set of curvilinear coordinates associated to the airfoil surface. In particular, $\boldsymbol{s} = (s_1, s_2)$ and n are the coordinates along the streamwise, cross-flow, and outward normal to the airfoil directions, respectively. Also, the unit vectors associated to these coordinates are denoted by $\hat{\boldsymbol{s}}_1$, $\hat{\boldsymbol{s}}_2$ and $\hat{\boldsymbol{n}}$, respectively. Unlike the actual velocity, this pseudo-velocity asymptotes to a constant outside the boundary layer, even with strong curvature, thus making the edge of the boundary layer a well-defined location. In particular, the BL edge n_e is defined as the first location along n-direction simultaneously satisfying

$$|\bar{\boldsymbol{\omega}}|\, n \le \epsilon_1 \,|\bar{\boldsymbol{v}}^*|, \qquad\qquad \left|\frac{\partial \bar{\boldsymbol{\omega}}}{\partial n}\right| n^2 \le \epsilon_2 \,|\bar{\boldsymbol{v}}^*|, \tag{24}$$

where $\epsilon_1 = 0.01$ and $\epsilon_2 = 0.1$ are some properly tuned constants for a systematic and robust detection of the BL edge, and the overbar denotes temporal and cross-flow averaging, i.e.,

$$\bar{\boldsymbol{\omega}}(s_1, n) := \frac{1}{T \cdot \Delta s_2} \int_0^T \int_0^{\Delta s_2} \boldsymbol{\omega}(\boldsymbol{s}, n, t)\, ds_2\, dt. \tag{25}$$

Cross-flow averaging corresponds to ensemble averaging due to the quasi-2D nature of the geometry and boundary conditions in the Eppler 387 wing, and is therefore used to accelerate statistical output convergence.

The local streamwise and cross-flow unit vectors above are defined as

$$\hat{\boldsymbol{s}}_1(s_1) := \bar{\boldsymbol{v}}_e/\bar{v}_e, \qquad\qquad \hat{\boldsymbol{s}}_2(s_1) := \hat{\boldsymbol{s}}_1 \times \hat{\boldsymbol{n}}, \tag{26}$$

where $\bar{\boldsymbol{v}}_e = \overline{\boldsymbol{v}^*(n_e)}$ is the pseudo-velocity at the edge of the boundary layer and $\bar{v}_e = |\bar{\boldsymbol{v}}_e|$ is its magnitude. Also, the average $\bar{v}_1$ and fluctuating v_1' streamwise velocities are given by

$$\bar{v}_1(s_1, n) = \bar{\boldsymbol{v}}^*(s_1, n) \cdot \hat{\boldsymbol{s}}_1(s_1, n), \qquad v_1'(\boldsymbol{s}, n, t) := v_1(\boldsymbol{s}, n, t) - \bar{v}_1(s_1, n), \tag{27}$$

whereas the streamwise displacement thickness, momentum thickness, and shape parameter read as

$$\delta^*(s_1) := \int_0^{n_e} \left(1 - \frac{\bar{v}_1}{\bar{v}_e}\right) dn, \qquad\qquad \theta(s_1) := \int_0^{n_e} \left(1 - \frac{\bar{v}_1}{\bar{v}_e}\right) \frac{\bar{v}_1}{\bar{v}_e}\, dn, \qquad\qquad H(s_1) := \frac{\delta^*}{\theta}. \tag{28}$$

The amplitude A_1 and amplification factor N_1 of streamwise perturbations at the boundary layer location s_1 are given by

$$A_1(s_1) = \frac{1}{\bar{v}_e \sqrt{n_e}} \sqrt{\int_0^{n_e} \overline{v_1'^2}\, dn}, \qquad N_1(s_1) := \ln\left(\frac{A_1(s_1)}{A_{1,0}}\right), \tag{29}$$

where $A_{1,0}$ is some reference amplitude. We note that $A_{1,0}$ shifts $N_1(s_1)$ by a constant factor but it does not affect its growth rate. The cross-flow version of the previous quantities are defined in an analogous manner.

C.   Kinetic energy, entropy and numerical dissipation in the TGV problem

The dissipation rate of integrated kinetic energy in the TGV problem, $E_k = \int_\Omega \rho\, |\boldsymbol{v}|^2/2$, is given by

$$-\frac{dE_k}{dt} = \epsilon_1 + \epsilon_2, \tag{30}$$

where

$$\epsilon_1 = \int_\Omega \Phi = \int_\Omega \nabla \boldsymbol{v} : \boldsymbol{\tau}, \qquad\qquad \epsilon_2 = -\int_\Omega p\, (\nabla \cdot \boldsymbol{v}), \tag{31}$$

are the viscous dissipation and pressure dilatation terms, respectively, and where : denotes the Frobenius inner product. For a Newtonian fluid,

$$\epsilon_1 = \int_\Omega \mu\, |\boldsymbol{w}|^2 + \int_\Omega (\lambda + 2\mu)(\nabla \cdot \boldsymbol{v})^2 = \epsilon_{1,a} + \epsilon_{1,b}, \tag{32}$$

where λ denotes the second coefficient of viscosity. In the incompressible limit, $\nabla \cdot \boldsymbol{v} = 0$ and thus

$$-\frac{dE_k}{dt} = \epsilon_{1,a} = 2\frac{\mu}{\rho}\mathcal{E} \ge 0, \tag{33}$$

American Institute of Aeronautics and Astronautics

where $\mathcal{E} = \int_\Omega \rho \, |\boldsymbol{w}|^2 / 2$ is the integrated enstrophy. Also, the time evolution of integrated entropy in the TGV problem, $S = \int_\Omega \rho s$, is given by

$$\frac{dS}{dt} = \epsilon_3 + \epsilon_4, \tag{34}$$

where

$$\epsilon_3 = \int_\Omega k \frac{|\nabla T|^2}{T^2} \geq 0, \qquad\qquad \epsilon_4 = \int_\Omega \frac{\Phi}{T} \geq 0. \tag{35}$$

We then define the numerical dissipation of the discretization scheme based on the compressible kinetic energy equation, the incompressible kinetic energy equation and the entropy equation as

$$\Pi_{E_k}^c := -\frac{dE_k}{dt} - \epsilon_1 - \epsilon_2, \qquad \Pi_{E_k}^i := -\frac{dE_k}{dt} - \epsilon_{1,a}, \qquad \Pi_S := \frac{dS}{dt} - \epsilon_3 - \epsilon_4, \tag{36}$$

respectively. All the time derivatives in this appendix are to be computed with the same time integration scheme as that used in LES.

References

[1] R. Alexander, Diagonally implicit Runge-Kutta methods for stiff ODEs, SIAM J. Numer. Anal. 14 (6) (1977) 1006–1021.

[2] T.J. Barth, Numerical Methods for Gasdynamic Systems on Unstructured Meshes, In: D. Kroner, M. Ohlberger,C. Rohde, C. (eds.), An Introduction to Recent Developments in Theory and Numerics for Conservation Laws, Lecture Notes in Computational Science and Engineering, vol. 5, pp. 195–285. Springer, Berlin (1999).

[3] P. Billingsley, Probability and Measure, John Wiley & Sons, 3rd ed., New York, 1995.

[4] J.P. Boris, On Large Eddy Simulation using subgrid turbulence models, In: Whither Turbulence. Turbulence at the Crossroads, J.L. Lumley, (ed.), Springer, pp. 344–353, New York, 1990.

[5] M.E. Brachet, Direct simulation of three-dimensional turbulence in the Taylor-Green vortex, Fluid Dyn. Res. 8 (1–4) (1991) 1–8.

[6] X.C. Cai, M. Sarkis, A restricted additive Schwarz preconditioner for general sparse linear systems, SIAM J. Sci. Comput. 21 (2) (1999) 792–797.

[7] B. Cockburn, J. Gopalakrishnan, R. Lazarov, Unified hybridization of discontinuous Galerkin, mixed and continuous Galerkin methods for second order elliptic problems, SIAM J. Numer. Anal. 47 (2) (2009) 1319–1365.

[8] B. Cockburn, J. Guzman, S.C. Soon, H.K. Stolarski, An Analysis of the Embedded Discontinuous Galerkin Method for Second-Order Elliptic Problems, SIAM J. Numer. Anal. 47 (4) (2009) 2686–2707.

[9] P. Fernandez, N.C. Nguyen, X. Roca, J. Peraire, Implicit large-eddy simulation of compressible flows using the Interior Embedded Discontinuous Galerkin method, In: 54th AIAA Aerospace Sciences Meeting, San Diego, USA, 2016.

[10] P. Fernandez, High-Order Implicit-Large Eddy Simulation for Transitional Aerodynamic Flows, Master Thesis, Department of Aeronautics and Astronautics, Massachusetts Institute of Technology, 2016.

[11] P. Fernandez, N.C. Nguyen, J. Peraire, The hybridized Discontinuous Galerkin method for Implicit Large-Eddy Simulation of transitional turbulent flows, J. Comput. Phys. 336 (1) (2017) 308–329.

[12] A. Frere, K. Hillewaert, H. Sarlak, R.F. Mikkelsen, Cross-Validation of Numerical and Experimental Studies of Transitional Airfoil Performance, In: 33rd ASME Wind Energy Symposium, Kissimmee, USA, 2015.

[13] C. Fureby, G. Taylor, H.G. Weller, A.D. Gosman, A comparative study of subgrid scale models in homogeneous isotropic turbulence, Phys. Fluids 9 (5) (1997) 1416–1429.

[14] C. Fureby, F.F. Grinstein, Large Eddy Simulation of High-Reynolds-Number Free and Wall-Bounded Flows, J. Comput. Phys. 181 (1) (2002) 68–97.

[15] C. Fureby, N. Alin, N. Wikstrom. S. Menon, N. Svanstedt, L. Persson, Large-Eddy Simulation of High-Reynolds-Number Wall-Bounded Flows, AIAA J. 42 (3) (2004) 457–468.

[16] M.C. Galbraith, M.R. Visbal, Implicit Large-Eddy Simulation of low Reynolds number flow past the SD7003 airfoil, In: 46th AIAA Aerospace Sciences Meeting and Exhibit, Reno, USA, 2008.

[17] T.B. Gatski, J.P. Bonnet, Compressibility, Turbulence and High Speed Flow, Elsevier Science, 2009.

[18] F.F. Grinstein, C.R. DeVore, Dynamics of coherent structures and transition to turbulence in free square jets, Phys. Fluids 8 (5) (1996) 1237–1251.

[19] D. Knight, G. Zhou, N. Okong'o, V. Shukla, Compressible large eddy simulation using unstructured grids, In: 36th AIAA Aerospace Sciences Meeting and Exhibit, Reno, USA, 1998.

[20] M. Lee, R. Moser, Direct numerical simulation of turbulent channel flow up to $Re_\tau \approx 5200$, J. Fluid Mech. 774 (2015) 395–415.

[21] J.E.W. Lombard, D. Moxey, S.J. Sherwin, J.F.A. Hoessler, S. Dhandapani, M.J. Taylor, Implicit Large-Eddy Simulation of a Wingtip Vortex, AIAA J. 54 (2) (2016) 506–518.

[22] D.K. Lilly, The representation of small-scale turbulence in numerical simulation experiments, In: Proc. IBM Scientific Computing Symposium on Environmental Sciences, p. 195, 1967.

[23] R.J. McGhee, B.S. Walker, B.F. Millard, Experimental Results for the Eppler 387 Airfoil at Low Reynolds Numbers in the Langley Low-Turbulence Pressure Tunnel, NASA Technical Memorandum 4062, Langley Research Center, 1988.

[24] R.C. Moura, S. Sherwin, J. Peiró, Linear dispersion-diffusion analysis and its application to under-resolved turbulence simulations using discontinuous Galerkin spectral/hp methods, J. Comp. Phys. 298 (2015) 695–710.

[25] R.C. Moura, G. Mengaldo, J. Peiró, S. Sherwin, On the eddy-resolving capability of high-order discontinuous Galerkin approaches to implicit LES / under-resolved DNS of Euler turbulence, J. Comp. Phys. 330 (1) (2017) 615–623.

[26] S.M. Murman, L.T. Diosady, A. Garai, M. Ceze, A Space-Time Discontinuous-Galerkin Approach for Separated Flows, In: 54th AIAA Aerospace Sciences Meeting, San Diego, USA, 2016.

[27] N.C. Nguyen, J. Peraire, Hybridizable discontinuous Galerkin methods for partial differential equations in continuum mechanics, J. Comput. Phys. 231 (18) (2012) 5955–5988.

[28] N.C. Nguyen, J. Peraire, B. Cockburn, A class of embedded discontinuous Galerkin methods for computational fluid dynamics, J. Comput. Phys. 302 (1) (2015) 674–692.

[29] F. Nicoud, F. Ducros, Subgrid-scale stress modeling based on the square of the velocity gradient tensor, Flow Turb. & Comb. 62 (1999) 183–200.

[30] J.S. Park, F.D. Witherden, P.E. Vincent, High-Order Accurate Implicit Large Eddy Simulations of Flow over a NACA0021 Aerofoil in Deep Stall, AIAA J., Accepted for Publication.

[31] J. Peraire, N.C. Nguyen, B. Cockburn, A hybridizable discontinuous Galerkin method for the compressible Euler and Navier-Stokes equations, In: 48th AIAA Aerospace Sciences Meeting, Orlando, USA, 2010.

[32] J. Peraire, N.C. Nguyen, B. Cockburn, An Embedded Discontinuous Galerkin Method for the Compressible Euler and Navier-Stokes Equations, In: 20th AIAA Computational Fluid Dynamics Conference, Honolulu, USA, 2011.

[33] F. Renac, M. de la Llave Plata, E. Martin, J.-B. Chapelier, V. Couaillier, Aghora: A High-Order DG Solver for Turbulent Flow Simulations, In: IDIHOM: Industrialization of High-Order Methods - A Top-Down Approach, Notes on Numerical Fluid Mechanics and Multidisciplinary Design 128 (2015) 315–335.

[34] P.L. Roe, Approximate Riemann solvers, parameter vectors, and difference schemes, J. Comput. Phys. 43 (1981) 357-372.

[35] Y. Saad, M.H. Schultz, GMRES: A Generalized Minimal Residual Algorithm for Solving Nonsymmetric Linear Systems, SIAM J. Sci. Stat. Comput. 7 (3) (1986) 856–869.

[36] J. Smagorinsky, General circulation experiments with the primitive equations. I. The basic experiment, Mon. Weather Rev. 91 (1963) 99–164.

[37] P.R. Spalart, Strategies for turbulence modelling and simulations, Int. J. Heat Fluid Fl. 21 (2000) 252–263.

[38] G.I. Taylor, A.E. Green, Mechanism of the production of small eddies from large ones, P. R. Soc. Lond. A. 158 (1937) 499–521.

[39] A. Uranga, P.-O. Persson, M. Drela, J. Peraire, Implicit Large Eddy Simulation of transition to turbulence at low Reynolds numbers using a Discontinuous Galerkin method, Int. J. Numer. Meth. Eng. 87 (2011) 232–261.

[40] W.M. van Rees, A. Leonard, D.I. Pullin, P. Koumoutsakos, A comparison of vortex and pseudo-spectral methods for the simulation of periodic vortical flows at high Reynolds numbers, J. Comput. Phys. 230 (8) (2011) 2794–2805.

[41] M.R. Visbal, R.E. Gordnier, M.C. Galbraith, High-fidelity simulations of moving and flexible airfoils at low Reynolds numbers, Exp. Fluids 46 (5) (2009) 903–922.

[42] A.W. Vreman, An eddy-viscosity subgrid-scale model for turbulent shear flow: Algebraic theory and applications, Phys. Fluids 16 (2004) 3670–3681.

[43] A. Yoshizawa, Statistical theory for compressible turbulent shear flows, with the application to subgrid modeling, Phys. Fluids A 29 (1986) 2152–2164.

[44] C.C. de Wiart, K. Hillewaert, Development and Validation of a Massively Parallel High-Order Solver for DNS and LES of Industrial Flows, In: IDIHOM: Industrialization of High-Order Methods - A Top-Down Approach, Notes on Numerical Fluid Mechanics and Multidisciplinary Design 128 (2015) 251–292.

[45] Y. Zhou, Z.J. Wang, Implicit Large Eddy Simulation of Transitional Flow over a SD7003 Wing Using High-Order Spectral Difference Method, In: 40th Fluid Dynamics Conference and Exhibit, Chicago, USA, 2010.